Bacterial Nitric Oxide Reductase (NorBC) Models Employing Click Chemistry

Jill B. Harland, a Subhra Samanta, a,b Nicolai Lehnert*a

^a Department of Chemistry, The University of Michigan, Ann Arbor, Michigan 48109-1055, United States

Dedicated to the memory of F. Ann Walker.

Keywords: nitric oxide, click chemistry, model complexes, bacterial nitric oxide reductase, spectroscopy, dinitrosyl iron complexes

^b Current address: Material Processing & Microsystem Laboratory. CSIR- Central Mechanical Engineering Research Institute, Durgapur, India

Abstract.

Bacterial NO Reductase (NorBC or cNOR) is a membrane-bound enzyme found in denitrifying bacteria that catalyzes the two-electron reduction of NO to N₂O and water. The mechanism by which NorBC operates is highly debated, due to the fact that this enzyme is difficult to work with, and no intermediates of the NO reduction reaction could have been identified so far. The unique active site of NorBC consists of a heme b₃/non-heme Fe_B diiron center. Synthetic model complexes provide the opportunity to obtain insight into possible mechanistic alternatives for this enzyme. In this paper, we present three new synthetic model systems for NorBC, consisting of a tetraphenylporphyrin-derivative clicked to modified BMPA-based ligands (BMPA = bis(methylpyridyl)amine) that model the non-heme site in the enzyme. These complexes have been characterized by EPR, IR and UV-Vis spectroscopy. The reactivity with NO was then investigated, and it was found that the complex with the BMPA-carboxylate ligand as the non-heme component has a very low affinity for NO at the non-heme iron site. If the carboxylate functional group is replaced with a phenolate or pyridine group, reactivity is restored and formation of a diiron dinitrosyl complex was observed. Upon one-electron reduction of the nitrosylated complexes, following the semireduced pathway for NO reduction, formation of dinitrosyl iron complexes (DNICs) was observed in all three cases, but no N₂O could be detected.

1. Introduction

Nitrogen is a crucial building block for essential biomolecules and is a key nutrient for all life forms. The nitrogen cycle is a major biogeochemical process that is essential to life on Earth and encompasses the conversion of nitrogen into its various forms in the environment.¹⁻⁵ Gaseous dinitrogen (N₂) constitutes 78% of our atmosphere and represents the major source of Earth's available nitrogen. In order for this source of nitrogen to be utilized by plants and microorganisms, N₂ must be fixed first into other forms, especially ammonia (NH₃)/ammonium (NH₄⁺). N₂ is fixed on a large scale by microorganisms that live symbiotically with leguminous plants. Humans have supplemented natural N₂ fixation with the Haber-Bosch process, where hydrogen gas (H₂) and N₂ are combined at high pressure and temperature over a Fe-based catalyst to produce NH₃.⁶⁻⁸ Overfertilization is a common practice in developed countries where fertilizers containing NH₃/NH₄⁺ and NO₃⁻ are cheap and abundant. Plants only take up 30-50% of all nitrogen fertilizer in the soil, leaving the rest to be metabolized by soil and seawater dwelling microbes. 9-12 Nitrification is the process of oxidation of ammonium to nitrite (NO₂⁻) and nitrate (NO₃⁻) and is carried out by autotrophic ammonia oxidizing bacteria (AOB)¹³⁻¹⁵ and archaea (AOA)¹⁶⁻¹⁸. NH₃ is oxidized by six electrons to NO2- with hydroxylamine (NH2OH) and nitric oxide (NO) as intermediates, ^{10,19,20} with the goal of obtaining reducing equivalents for respiration, thereby providing substrate for nitrite-oxidizing bacteria (NOB). 15,21,22 Another pathway involves "complete ammonia-oxidizing" (COMAMMOX) bacteria, which perform an eight electron oxidation of ammonia to nitrate, utilizing similar enzymes as those found in AOBs and NOBs. 23,24 NO₃⁻ and NO₂⁻ have low retention in the soil and leach into the waterways as pollutants, causing downstream eutrophication leading to algae blooms in lakes and coastal waters.²⁵ On the other hand, anaerobic soil-dwelling bacteria and fungi convert NO₂⁻ and NO₃⁻ into nitrous oxide (N₂O) in fungal and N₂ in bacterial denitrification, where NO is a key intermediate. ^{26,27} Approximately 75% of anthropogenic N₂O emissions are a result of microbial and fungal denitrification. While bacterial denitrification can yield N₂, a large portion of the N₂O intermediate can escape before being further reduced. N₂O is the third most important greenhouse gas, by means of radiation trapped in the atmosphere, after CO₂ and methane. ²⁸ The N₂O results from the two-electron reduction of NO catalyzed by respiratory NO reductases (NORs), which is a key step in denitrification. Fungal NOR enzymes are a part of the Cytochrome (Cyt.) P450 enzyme superfamily, whereas, in contrast, bacterial NORs are related to the heme-copper oxidase family, which also includes Cyt. c oxidases.²⁹ Bacterial NOR (NorBC or cNOR) is a periplasmic membrane-bound enzyme that is purified from members of the *Pseudomonas* family. ^{30,31} NorBC is a non-electrogenic heterodimer ($\alpha\beta$), with the smaller subunit, NorC, containing a low-spin (ls) heme c axially coordinated by His and Met residues, which is responsible for receiving electrons from Cyt. c and transferring them to the NorB subunit. 32,33 NorB is the larger subunit that spans the cytoplasmic membrane. The bimetallic active site of NorBC along with a ls heme b with bis-His coordination, which is responsible for electron transfer to the active site, is housed in the NorB subunit. 33 The active site features two different types of iron sites, a heme b_3 center and a nonheme iron center termed Fe_B. Heme b_3 is ligated by an axial His and Fe_B is coordinated by three His residues and a Glu side chain. In addition, in the resting state of *Pseudomonas aeruginosa* (*Pa*) NorBC, an oxo bridge is present that connects the two Fe centers as shown in the crystal structure of this enzyme in Figure 1B. 34,35

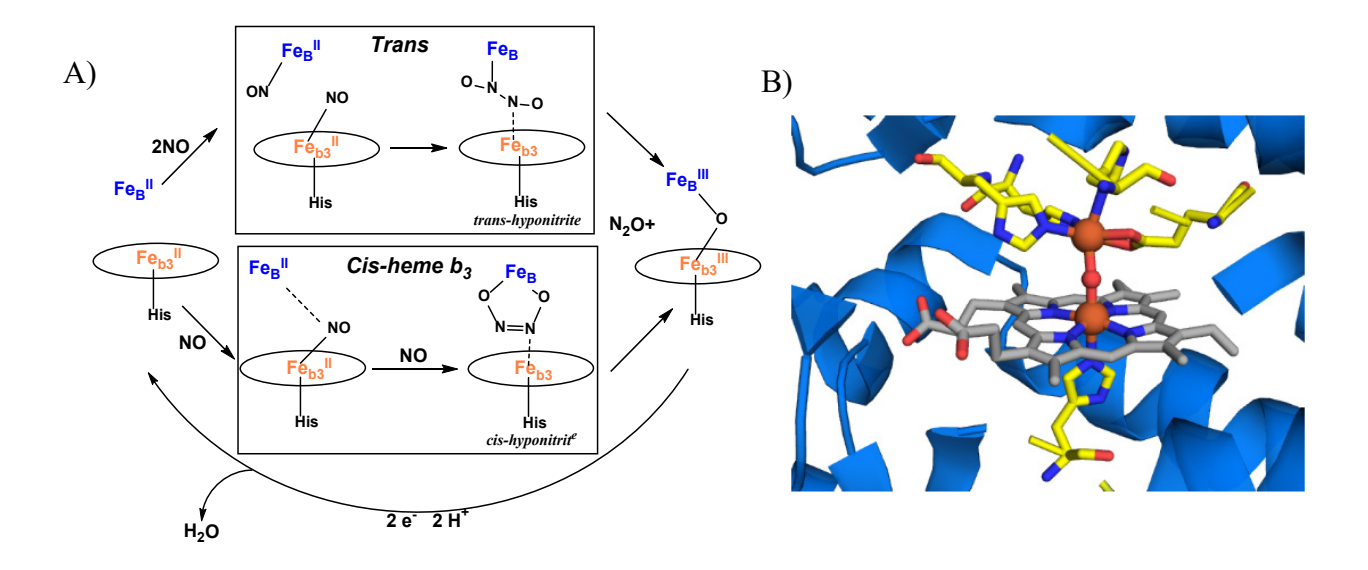


Figure 1. (A) Proposed mechanisms for NorBC, with the *trans* mechanism shown on the top and the *cis*-heme b_3 mechanism on the bottom. (B) PyMOL image of the diiron Pa NorBC active site (PDB: 300R).

NorBC is notoriously hard to work with, due to the fact it is an integral membrane protein and difficult to express, purify, and crystallize. Thus, its mechanism of action is still unknown. Based on current data, there are two main proposed mechanisms, shown in Figure 1A.⁴ The first mechanism, termed the *trans*-mechanism, has both iron sites binding one NO molecule, followed by a radical-type N-N coupling reaction, generating a *trans*-hyponitrite intermediate. After N₂O release, the two ferric iron centers are bridged by an oxo group.³⁶ The proposed hyponitrite intermediate has never been observed spectroscopically. Additionally, computational studies from the Blomberg group have shown that the *trans*-mechanism is highly unfavorable and has an activation barrier for N-N bond formation that is prohibitively high.³⁷ The second mechanism, termed *cis*-heme *b*₃, is inspired by findings for Cyt. P450nor.³⁸⁻⁴⁰ In this mechanism, the first

molecule of NO binds to the heme b_3 site, forming a low-spin (ls-) {FeNO}⁷ complex, and the Fe_B center acts as Lewis acid and interacts with the O atom of the bound NO unit to electrostatically polarize the NO ligand, giving it more ¹NO⁻ character. Here we use the Enemark-Feltham notation, $\{Fe(NO)_x\}^n$, where x is the number of coordinated NO ligands and n is the number of valence electrons (Fe(d) + NO(π *) electrons, here n = 7).⁴¹ In the proposed mechanism, the second NO molecule then directly attacks the heme-bound NO ligand to form a cis-hyponitrite intermediate. N₂O is released and the diferric, oxo-bridged active site results.^{37,42} Computations show this to be the most energetically favorable mechanism proposed for NorBC.³⁷ A third mechanism, termed the cis-FeB mechanism, has both NO molecules binding to the FeB site, but this mechanism is widely discounted due to several reasons, including that a corresponding dinitrosyl iron complex (DNIC) is unlikely to form in the presence of heme, which has a strong affinity for NO, ^{43,44} and the fact that N-N coupling in a DNIC is a highly spin-forbidden reaction.⁴⁴ Recently, utilizing time-resolved UV-Vis and IR spectroscopy (for N₂O detection) in combination with a photosensitive, caged NO donor, three stages of NO binding to Pa cNOR were identified. First, on the microsecond timescale, NO enters the active site and binds to the non-heme iron(II) center, forming a high-spin (hs-) {FeNO}⁷ complex. Then, on the tens of microseconds timescale, NO migrates to form a possible 5C heme b_3 -NO complex. Finally, on the millisecond timescale, a second NO molecule enters the active site, leading to protonation and electron transfer to promote N-N bond formation, N-O bond cleavage, and N₂O formation. 45,46

Model complexes and protein models have been useful tools in probing NO intermediates and help give mechanistic clues for NorBC, since this enzyme is so difficult to work with (Figure 2). Some of the first heme/non-heme model complexes of NorBC came out of the Karlin group. Here, a tetraphenylporphyrin (TPP) derivative, used as the heme component, is covalently linked to a

tris(methylpyridyl)amine (TMPA) derivative as an Fe_B site mimic.⁴⁷ This complex is able to form a diferrous dinitrosyl complex, but does not form N₂O. A variety of different heme and non-heme iron components have subsequently been developed, leading to the determination of benchmark spectroscopic data for diiron dinitrosyl species.⁴⁸⁻⁵³ The heme **ls**-{FeNO}⁷ component usually shows N-O stretching frequencies ranging from 1620-1700 cm⁻¹, while those of the non-heme **hs**-{FeNO}⁷ component range from 1720-1810 cm⁻¹.⁵⁴⁻⁵⁶ The flexible aryl linkers employed in these compounds make it unclear how the heme/non-heme pieces interact and if they do at all. The first functional model complex for NorBC comes from the Collman group. A picket-fence porphyrin was modified to append three of the pickets with imidazole residues to form a second metal binding site.^{57,58} The diferrous version of this complex supports N₂O formation upon reaction with NO at room temperature.⁵² Low-temperature studies showed the possible generation of a heme/non-heme dinitrosyl species before N₂O formation, which would support the *trans*-mechanism. The synthesis of this complex is tedious and low yielding, so catalytic turnover of NO could not be achieved, nor could deeper mechanistic studies be conducted.

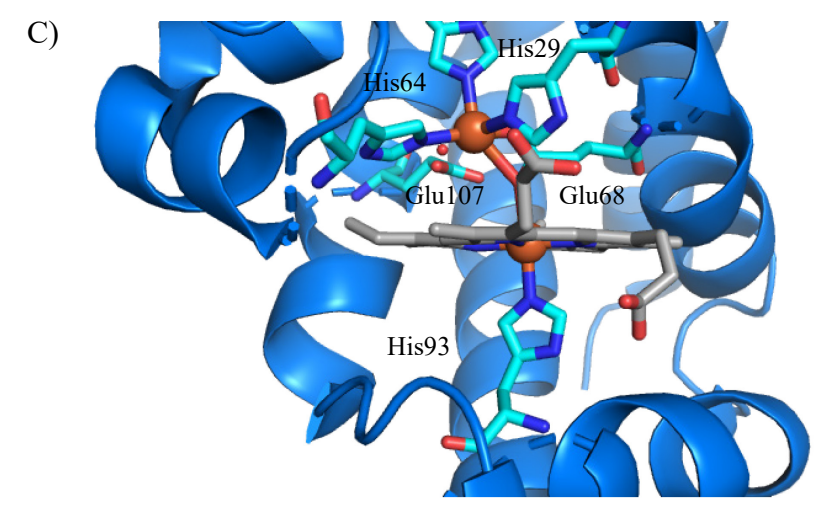


Figure 2. NorBC synthetic model complexes (A) from Karlin and coworkers and (B) from Collman and coworkers. (C) Lu and coworkers prepared several protein models of NorBC; shown here is Fe_BMb2 (PDB: 3M39).^{48,59,60}

In addition to synthetic model complexes, protein models have also been developed, specifically in the protein myoglobin (Mb). The Lu group engineered the distal pocket of sperm whale Mb to incorporate a non-heme binding site.⁶¹ The first generation, Fe_BMb1, has the mutations Leu29His, Phe43His, Val68Glu to create the non-heme iron site.^{62,63} The second generation, Fe_BMb2, has an additional Ile107Glu mutation, which induces an interaction of a water molecule with the Glu to form a hydrogen-bonding network in the active site.⁵⁹ Fe_BMb2 shows a 50% yield of N₂O in a productive single-turnover reaction with a rate constant of 0.7 s⁻¹ at 4 °C, which is twice as large as that for Fe_BMb1.⁵⁹ A diferrous dinitrosyl intermediate was detected with rapid freeze-quench-rRaman, and UV-Vis stop flow experiments, which suggests that the protein follows the *trans*-mechanism.⁵⁹ In the case of both the Mb model and Collman's complex, the large Fe-Fe distance compared to NorBC could facilitate the *trans*-mechanism. Follow-up studies on the Mb models where the non-heme metal is varied (Co, Zn, Cu) and the heme cofactor is replaced with heme derivatives of varying redox potentials were also conducted.^{64,65} Surprisingly, the model with the Zn²⁺ ion in the non-heme metal binding site retains reactivity, pointing to the

role of the non-heme metal as a Lewis acid as proposed in the *cis*-heme b_3 mechanism. ^{64,65} Despite the intense research on NorBC models, many mechanistic questions remain. Herein, we report three new NorBC model complexes that employ click chemistry, and we study the reactivity of these complexes with NO.

2. Experimental Section

General Methods

Air sensitive materials were handled and prepared under inert conditions (N₂ or Ar gas) using standard Schlenk techniques, or in an MBraun glovebox equipped with a circulating purifier (O₂, H₂O <0.1 ppm). All solvents were dried using standard techniques, freeze-pump-thawed to remove O₂, and stored over activated molecular sieves (3 or 4 Å). All reagents were purchased from commercial sources and were used as received, unless noted below. Zn/Hg amalgam⁶⁶ and [Fe(BF₄)₂]·2.5(CH₃CN)⁶⁷ were prepared according to literature procedures. Nitric oxide (NO; Cryogenic Gases, Inc., 99.5%) was purified by passage through an ascarite II column (NaOH on silica), followed by a cold trap at -80 °C to remove higher-order nitrogen oxide impurities. ¹⁵NO was prepared according to literature procedures. ⁶⁸ Cobaltocene (CoCp₂) was sublimed under static vacuum and stored at -35 °C in the glovebox freezer.

Physical Measurements

UV-Vis Spectroscopy

All UV-Vis spectra were recorded using an Analytik Jena Specord S600 spectrometer. Typical concentrations of the complexes for UV-Vis experiments were ~6 μM.

IR(ATR/KBr/Gas) Spectroscopy

Solution IR spectra were taken on a Bruker Alpha-E FTIR spectrometer. Solution samples were measured in a thin-layer solution cell equipped with CaF₂ windows. Solid and gas-phase IR spectra were taken on a Thermo-Nicolet IS-50 benchtop IR spectrometer. Gas samples were measured using a Pike HT gas cell (10 cm) with CaF₂ windows.

Cyclic Voltammetry

Cyclic voltammograms (CVs) were obtained on a CH Instruments CHI600E electrochemical workstation with a glassy-carbon working electrode, platinum counter electrode, and silver wire pseudoreference electrode. All potentials were referenced to a ferrocene (Fc) standard taken after each experiment under the same experimental conditions. Data were collected on ~5 mM samples in either CH₂Cl₂ or CH₃CN with 0.1 M tetrabutylammonium hexafluorophosphate as the supporting electrolyte.

EPR Spectroscopy

Electron paramagnetic resonance (EPR) spectra were obtained on a Bruker X-band EMX spectrometer, equipped with an Oxford Instruments liquid-helium or liquid-nitrogen cryostat. Spectra were taken at 4 K or 100 K, with 20 mW microwave power and 1 G modulation amplitude with a sample concentration of 1 mM, unless otherwise stated. The g values and signal integrals were obtained using the program SpinCount (by Prof. M. P. Hendrich, Carnegie Mellon University). Quantification of the amount of heme-nitrosyl formed was performed by comparison to an authentic sample of [Fe(TPP)(NO)] at the same concentration, via double integration of the EPR signals.

NMR Spectroscopy

Proton NMR spectra were recorded on a Varian MR 400 MHz instrument or a Varian NMRS 500 MHz spectrometer at room temperature (20 - 22 °C). All spectra were referenced to internal deuterated solvent peaks.

Mass Spectrometry

Mass spectrometry (MS) data were collected on an Agilent 6230 time-of-flight high-performance liquid chromatography/mass spectrometer.

Elemental Analysis

Elemental Analyses (EAs) were conducted by Atlantic Microlabs (Norcross, GA).

N₂O Yield Tests

N₂O tests were performed as previously described.⁶⁹ 9μmol of complex was dissolved in 2.5 mL of CH₂Cl₂ in a 25 mL round-bottom flask with a septum. 2 mL of NO gas was added via a bomb flask and syringe. The reaction mixture was stirred for various times before transferring the headspace into an evacuated gas-IR cell for exactly 20 sec via a cannula. The N₂O band, if present, was integrated from 2150 to 2275 cm⁻¹ after the subtraction of a CH₂Cl₂ blank taken under the exact same conditions, and the integral of the signal was compared to a stand curve. Similarly, for the chemical reduction experiment, 9μmol of complex was dissolved in 2 mL of CH₂Cl₂ in a 25 mL round-bottom flask. 1 equiv of CoCp₂ was dissolved in 0.5 mL of CH₂Cl₂ and added to the round-bottom flask. The same procedure was then followed as described above.

Synthetic Procedures

Synthesis of the Heme Precursor

5-(4-nitrophenyl)-10,15,20-triphenylporphyrin (H₂[m-NO₂TPP]; m = mono). A 3,000 mL 3-neck round-bottom flask was equipped with a stir bar, reflux condenser, glass stopper, and an addition funnel. Nitrobenzaldehyde (7.6 g, 1 equiv) was transferred to the flask. 800 mL of propionic acid was measured out in a graduated cylinder and added to the flask, followed by the addition of benzaldehyde (16.0 g, 3 equiv) by syringe. The solution was brought to a boil for ~10 min. Pyrrole (20.9 mL, 6 equiv) was freshly distilled (same day) and loaded into the addition funnel. The heat was lowered to just below boiling and the pyrrole was added slowly dropwise at a continuous rate. The solution turned from yellow to dark red/brown upon addition of pyrrole. The solution was brought back up to reflux and refluxed for ~30-40 min. A precipitate could be seen forming on the sides of the flask during reflux. The flask was cooled to room temperature. A purple solid was collected by vacuum filtration, then washed with hexanes. This yielded a mixture of H₂[TPP] and H₂[m-NO₂TPP]. Two spots can be seen on a TLC plate (50:50 CH₂Cl₂/Hexanes) corresponding to the two products formed. Dried crude product was taken straight into the next reaction without further purification, so no yield was determined.

5-(4-aminophenyl)-10,15,20-triphenylporphyrin (H₂[m-NH₂TPP]; m = mono). In a 2 L beaker charged with a stir bar, the crude solid of H₂[m-NO₂TPP] was dissolved in ~150 mL CH₂Cl₂. 100 mL of concentrated HCl was added and the dark purple solution turned blue/green. SnCl₂ (27.5 g, 6 equiv (6-10 equiv can be used)) was added to the beaker. The beaker was covered with a piece of paper and the reaction mixture was stirred overnight. The resulting solution was then placed in

an ice bath. ~150 mL of DI water was added to the solution. Ammonia was added until the solution was neutralized, as verified by pH paper. The solution turned purple upon neutralization. Liquid-liquid extraction (LLE) with CH₂Cl₂/DI water was performed until all the excess SnCl₂ was removed and the water layer was mostly clear. The CH₂Cl₂ layer was then washed with a saturated solution of NaCl in water (~200 mL). The CH₂Cl₂ layer was collected and dried with sodium sulfate. Next, the solvent was removed by rotary evaporation to yield a purple solid. A 2.5 ft tall and 8-inch-wide column was wet packed with 1.5 ft tall of silica in CH₂Cl₂. ~1/3 of the crude product was dry loaded onto the column. 40:60 CH₂Cl₂/Hexanes was used to elute H₂[TPP] as a large dark purple band. Next, a yellow/orange band was eluted and discarded. The eluting solvent was switched to 100% CH₂Cl₂ to elute a pink product band. Yield: 645 mg, 9 %. ¹H-NMR (CDCl₃) $\delta = 8.89-8.84$ (8H, dd), 8.21 (6H, d), 7.89 (1H, d), 7.76 (9H, m), 7.59 (1H, t), 7.17 (1H, t), 7.11(1H, d), 3.54 (2H, s), -2.74 (2H, s). UV-Vis (CH₂Cl₂): 418, 514, 549, 589, 651 nm.

5-(4-azidophenyl)-10,15,20-triphenylporphyrin (H₂[m-N₃TPP]; m = mono). H₂[m-N₃TPP] was synthesized according to literature procedures with few modifications. H₂[m-NH₂TPP] (645 mg, 0.158 equiv) was dissolved in 130 mL of tetrahydrofuran (THF) and cooled in an ice bath. A saturated solution of NaNO₂ (70.7 mg, 0.158 equiv) in DI water was added, followed by H₂SO₄ (516 μL), and the solution turned green. The ice bath was removed and the solution was stirred for 30 min at room temperature. NaN₃ (73.3 mg, 0.174 equiv) in minimum water was added dropwise and bubbles evolved upon addition. The reaction was monitored by TLC and stirred for exactly 20 min. 130 mL of chloroform was added to the solution and then washed with DI water (200 mL, 3 times). The chloroform layer was collected, dried with sodium sulfate, and the solvent was removed by rotary evaporation. The crude product was purified by column chromatography.

Activated neutral alumina was used with 20% chloroform in hexanes as eluent. A yellow band elutes first followed by a large purple product band. Yield: 597 mg, 89%. 1 H-NMR (CDCl₃) δ = 8.85-8.83 (8H, m), 8.24-8.18 (8H, m), 7.84-7.76 (9H, m), 7.50 (2H, d), -2.74 (2H, s). UV-Vis (CH₂Cl₂): 417, 512, 549, 589, 643 nm. IR(ATR): ν (N₃) = 2122 cm⁻¹.

Metallation of 5-(4-azidophenyl)-10,15,20-triphenylporphyrin ([Fe(m-N₃TPP)(Cl)] and [Zn(m-N₃TPP)]). H₂[m-N₃TPP] (200 mg, 1 equiv) was dissolved in ~50 mL dimethylformamide (DMF) and ~10 mL of methanol (MeOH), followed by addition of FeCl₂ (77.4 mg, 2 equiv) or Zn(OAc)₂ (112 mg, 2 equiv). The solution was refluxed for 3-6 hrs. The solvent was removed by rotary evaporation and then the resulting solid was redissolved in CH₂Cl₂. A liquid-liquid extraction was then performed with water to remove excess salt. The product was then further purified by column chromatography. A silica column with 100% CH₂Cl₂ was used to elute unmetallated porphyrin. The solvent was then switched to 10% MeOH/CH₂Cl₂ to elute the metallated product (90% yield). Finally, the Fe product was washed with 1 M HCl to yield [Fe(m-N₃TPP)(Cl)]. [Fe(m-N₃TPP)(Cl)]: UV-Vis (CH₂Cl₂): 375, 417, 507, 577, 655 nm. EPR: effective g-values 6.0, 2.0. MS: m/z 709.17. IR(ATR): $v(N_3) = 2161$ cm⁻¹. [Zn(m-N₃TPP)]: UV-Vis (CH₂Cl₂): 420, 510, 548, 584 nm. ¹H-NMR (CDCl₃) δ = 8.96-8.90 (8H, m), 8.23-8.15 (8H, m), 7.87-7.73 (9H, m), 7.53 (2H, d). IR(ATR): $v(N_3) = 2156$ cm⁻¹. E_{1/2} values for [Fe(m-N₃TPP)(Cl)] are -0.80 V, -1.58 V, and -2.19 V (Figure S1).

Synthesis of the Non-heme Precursors

[(6-Bromo-2-pyridyl)methyl](2-pyridyl)methylamine. The procedure was adapted from the literature with slight modifications.⁷⁰ 50 mL of MeOH was added to a 500 mL round-bottom flask,

followed by the addition of Br-pyridine-2-aldehyde (2.36 g, 1 equiv). The flask was equipped with an addition funnel charged with picolylamine (1.54 mL, 1.2 equiv) in 10 mL of MeOH and added dropwise. The addition funnel was removed, the flask was capped, and the solution was stirred for 2 hrs. The solution was then cooled in an ice bath, and NaBH₄ (0.360 g, 0.75 equiv) was added slowly. The ice was removed and the flask was stirred at room temperature overnight. The following day the solvent was removed and the resulting orange oil was redissolved in ~50 mL CH₂Cl₂. The solution was then acidified with dilute HCl until the pH reached ~1-2. The solution turned pale yellow upon acidification. The organic layer was collected. 10 mL of 6 M NaOH was added to the acid layer and the solution turned white. ~50 mL of CH₂Cl₂ was added to the basified layer and the organic layer was collected and combined with the previous organic layer. The solvent was removed by rotary evaporation and the product was dried under vacuum overnight. Yield: 3.19 g, 86%. 1 H-NMR (CDCl₃) δ = 8.51 (1H, ddd), 7.60 (1H, td), 7.47 (1H, t), 7.33-7.29 (3H, m), 7.14-7.11 (1H, m), 3.92 (4H, s).

[(6-Bromo-2-pyridyl)methyl](2-pyridyl)methylamine – propionic acid (BMPA-Pr Br). [(6-bromo-2-pyridyl)methyl](2-pyridyl)methylamine (3.19 g, 1 equiv) was dissolved in ~45 mL MeOH and transferred to a 100 mL round-bottom flask. Methyl acrylate (1.2 mL, 1.2 equiv) was added to the flask and the solution was stirred for 3 days. The solvent was then removed and the obtained solid was redissolved in CH₂Cl₂. Liquid-liquid extraction with CH₂Cl₂/DI water was performed. The product was dried under vacuum overnight to yield a yellow oil. Yield: 4.04 g, 97%. 1 H-NMR (CDCl₃) δ = 8.51 (1H, ddd), 7.65 (1H, td), 7.46 (1H, t), 7.34-7.28 (3H, m), 7.12-7.09 (1H, m), 3.93-3.81 (4H, s), 3.60 (3H, s), 2.93-2.86 (2H, m), 2.54-2.49 (2H, m).

I(6-Bromo-2-pyridyl)methyl](2-pyridyl)methylamine – **phenol (BMPA-PhOH Br).** In a 50 mL round-bottom flask in the glovebox, [(6-Bromo-2-pyridyl)methyl](2-pyridyl)methylamine (4.0 g, 1 equiv) was dissolved in 20 mL dichloroethane. Salicylaldehyde (1.5 mL, 1.04 equiv) was added by syringe and the resulting solution was stirred for 3 hrs in the glovebox. Sodium triacetoxyborohydride (4.34 g, 1.5 equiv) was added to the flask and the solution was allowed to stir overnight in the glovebox. The next day the flask was removed from the glovebox and 60 mL of saturated sodium bicarbonate in DI water was added, and the solution was stirred for 45 min to quench the reaction. Liquid-liquid extraction with CH₂Cl₂/DI water (50 mL CH₂Cl₂, 3 times) was then performed. The organic layer was dried with sodium sulfate and the solvent was removed under rotary evaporation. The product was dried on the vacuum line overnight. Yield: 5.1 g, 98%. ¹H-NMR (CDCl₃) δ = 10.37 (1H, s), 8.57 (1H, ddd), 7.62 (1H, td), 7.44 (1H, t), 7.37 (1H, t), 7.30 (1H, t), 7.29-7.27 (3H, m), 7.19 (1H, d), 7.17-7.13 (1H, m), 6.84 (1H, d), 3.86 (2H, s), 3.82 (2H, s), 3.78 (2H, s).

[(6-Bromo-2-pyridyl)methyl]bis(2-pyridyl)methylamine (TMPA Br). To a stirred solution of [(6-bromo-2-pyridyl)methyl](2-pyridyl)methylamine (0.850 g, 1 equiv) in 25 mL of THF, picolylchloride hydrochloride (0.500 g, 1 equiv) was added, followed by the addition of triethylamine (851 μ L, 2 equiv). The solution was refluxed for 3 days. The reaction mixture was then cooled to room temperature and filtered. The filtrate was collected and the solvent was removed to obtain a red oil. The red oil was recrystallized overnight in a -20 °C freezer from ethyl acetate/CH₂Cl₂ (7:1) to yield a white solid. Yield: 0.850 g, 76%. ¹H-NMR (CDCl₃) δ = 8.54 (2H, ddd), 7.67 (4H, m), 7.59 (2H, td), 7.33 (1H, d), 7.16-7.13 (2H, m), 3.88 (6H, s).

Alkyne Addition Reaction. [(6-Ethynyl-2-pyridyl)methyl](2-pyridyl)methylamine—propionate (BMPA-Pr alkyne), [(6-Ethynyl-2-pyridyl)methyl](2-pyridyl)methylamine—phenol (BMPA-PhoH alkyne), and [(6-Ethynyl-2-pyridyl)methyl]bis(2-pyridyl)methylamine (TMPA alkyne) were all prepared by the same reaction, described below. The procedure to prepare BMPA-Pr alkyne is used as an example procedure.

BMPA-Pr Br (4.04 g, 1 equiv) was vacuum dried for 1 hr. Distilled ~50 mL triethylamine was degassed with Ar for 30 – 45 min before use and then put under a constant flow of Ar. BMPA-Pr Br was dissolved in a minimum amount of distilled THF and syringe transferred to the flask containing triethylamine. Pd(PPh₃)Cl₂ (0.45 g, 16.6 equiv) was added, followed by CuI (0.203 g, 0.1 equiv) to activate the Pd catalyst. The solution was stirred under Ar for 10 min and turned green. Trimethylsilylacetylene (3.03 mL, 2 equiv) was added and the solution turned bright yellow. The reaction was heated to 70 - 80 °C and stirred overnight. The solvent was removed and then the product was redissolved in CH₂Cl₂ and an liquid-liquid extraction was performed with DI water. The organic layer was collected and the solvent was removed by rotary evaporation. The product was purified by column chromatography. A silica column with 10% MeOH/CH₂Cl₂ was used to elute off product, which was the brown/orange second band. The product was dried overnight under vacuum to yield a brown solid. Yield: 0.96 g, 24%. This product (0.96 g, 1equiv) was then taken into a deprotection reaction to deprotect the alkyne. KF hydrate (1.7 g, 10 equiv) was added to a flask with product dissolved in a 50:50 mixture of THF/MeOH (75 mL each). The solution was stirred 6 - 8 hrs. Liquid-liquid extraction with CH₂Cl₂/DI water, followed by a brine wash of the organic layer, was then performed. The organic layer was then dried with sodium sulfate and the solvent was removed by rotary evaporation. Note: do not heat the product, as it can

easily polymerize. The product was characterized by ¹H-NMR, with the spectrum matching that of the parent brominated compound, except for the appearance of the alkyne proton as a new signal at ~4.0 ppm in CDCl₃.

Iron Metallation of BMPA-Pr alkyne, BMPA-PhOH alkyne, TMPA alkyne. The iron metallation procedure was the same for all of the three non-heme ligands. A general synthesis is given here. Except for the TMPA alkyne, the non-heme precursor (1 equiv) was dissolved in anhydrous THF with a saturated solution of NaOH (1 equiv) and refluxed at 70 °C for 3 hrs, in order to deprotonate the oxygen group (forming the propionate or phenolate group, respectively). The solvent was removed and the product was dried. In a glovebox, the resulting non-heme ligand was dissolved in a 1:1 mixture of CHCl₃/MeOH. FeCl₂ or Fe(OTf)₂ (10 equiv) was added to the reaction mixture, which was subsequently stirred for 1 hr. ~3x diethyl ether was added to precipitate the solid product, which was vacuum filtered (Yield: ~70%). In addition to the characterization described below, the iron-metallated complexes were also characterized by CV (Figure S1). The E_{1/2} values for the Fe^{III}/Fe^{II} couple of each complex follow the expected trend based on the functionalized arm's charge and donor strength. Thus, the E_{1/2} values are -254 mV for [Fe(TMPA alkyne)(Cl₂)], -366 mV for [Fe(BMPA-PhO alkyne)(Cl)], and -471 mV for [Fe(BMPA-Pr alkyne)(Cl)]. Measurements were generally conducted on 5 mM solutions of the complexes. Note that there is a difference in current observed, specifically for [Fe(TMPA alkyne)(Cl₂)]. This is likely due to the fact that the data were measured with different electrodes with vastly different capacitive (charging) currents, and correspondingly, different electron transfer kinetics at the electrode surface. The functional groups chosen here for the non-heme iron complexes provide a range of reduction potentials and coordination environments to explore in the clicked complexes described below. [Fe^{III}(BMPA-Pr alkyne)] (OTf)₂ UV-Vis (MeOH): 324 nm. [Fe^{II}(BMPA-Pr alkyne)] (OTf)Anal calcd for C₁₈H₁₆N₃O₅F₃SFe • CHCl₃ • C₄H₁₀O: C, 40.14; H, 3.96; N, 6.12. Found: C, 40.02; H, 4.14; N, 6.69. [Fe^{III}(TMPA alkyne)(Cl₂)] UV-Vis (MeOH): 361 nm. [Fe^{III}(BMPA-PhO alkyne)(Cl₂)] UV-Vis (MeOH): 332 nm. [Fe^{III}(BMPA-PhO alkyne)(Cl₂)] Anal calcd for C₂₁H₁₈N₃FeCl₂ • 2 CHCl₃ • CH₃OH: C, 40.98; H, 3.44; N, 6.04. Found: C, 40.60; H, 3.55; N, 6.21. EPR: effective g-values of Fe^{III} complexes: 4.3, 2.0.

Synthesis of Clicked Complexes

(M)heme-triazole(trz)-(M)non-heme (M = Fe, Zn). A general click reaction procedure from the literature was followed.⁷¹ H₂[m-N₃TPP] (1 equiv) was dissolved in THF (1:1 ratio of organic solvent to DI water), and the non-heme Fe alkyne complex (1.5 equiv) was dissolved in distilled MeOH and both were added to a round bottom flask. The flask was put under a constant flow of nitrogen. In a separate vial, CuSO₄·5H₂O (0.03 equiv) was dissolved in DI water. Solid sodium ascorbate (0.06 equiv) was added to the vial with CuSO₄·5H₂O₂, and the resulting mixture was then quickly added to the reaction flask. Sodium ascorbate activates the Cu catalyst and must be added when the Cu solution is dark brown (not when light brown or yellow). The reaction was stirred for 7 hrs at 50 °C. Liquid-liquid extraction with CH₂Cl₂/DI water was then conducted to stop the reaction. Column chromatography with silica gel using 60:40 CH₂Cl₂/Hexanes was used to elute the unclicked complexes, and then 10% MeOH/CH₂Cl₂ was used to elute the brown band of the clicked product. Note that the non-heme metal is removed in the process of column workup. For Fe heme metallated complexes a 1 M HCl wash was preformed to form the chloride-coordinated Fe heme complex. The clicked complexes were analyzed by IR spectroscopy, showing the disappearance of the azide stretch at 2122 cm⁻¹. UV-Vis spectroscopy can be used to analyze the

state of the heme component. The ¹H-NMR spectrum of the diamagnetic [Zn(TPP)-trz-(BMPA-Pr)] complex was used to characterize the complete clicked complex. Yield: 50-60% [Fe(TPP)(Cl)-trz-(BMPA-Pr)], [Fe(TPP)(Cl)-trz-(BMPA-PhOH)], [Fe(TPP)(Cl)-trz-(TMPA)]: UV-Vis (CH₂Cl₂): 378, 417, 508, 585, 686 nm.

[Zn(TPP)-trz-(BMPA-Pr)]: UV-Vis (CH₂Cl₂): 420, 550 nm. ¹H-NMR (CDCl₃) δ = 8.98-8.88 (8H, m), 8.60 (1H, ddd), 8.39-8.24 (8H, m), 7.98-7.84 (6H, m), 7.77 (9H, m), 7.66 (2H, m), 6.96 (1H, m), 3.57 (4H, s), 2.62 (2H, m), 2.30 (2H, m), 2.01 (3H, m).

Metallation of the Non-Heme Site and Nitrosylation of Clicked Complexes. During column workup (as described above), the metal bound to the non-heme site is removed, yielding [Fe^{III}(TPP)(C1)-trz-(non-heme)]. This allows for remetallation of the non-heme site with any desired metal ion. Procedure: [Fe^{III}(TPP)(Cl)-trz-(non-heme)] was dissolved in a minimal amount of CH₂Cl₂ and reduced with Zn/Hg amalgam (10 - 15 equiv). The heterogenous solution was stirred overnight in the glovebox (minimum: 12 hrs). The reduction of the complex was verified by UV-Vis spectroscopy (417, 443, 537, 617, 651, 647, 750 nm). These complexes were also analyzed by ¹H-NMR spectroscopy, as seen in Figures S8-S10. The solution was then filtered through a pipette with glass microfiber filter paper to remove the Zn/Hg amalgam. 1 equiv of the base 1,8-Diazabicyclo [5.4.0] undec-7-ene (DBU) was added to deprotonate the carboxylic acid or phenol arm, so that it can bind metals. Then, [Fe(BF₄)₂]·2.5(CH₃CN), Fe(OTf)₂, or Zn(OAc)₂ (2 equiv) was added to the solution and stirred for at least 1 hr to metallate the non-heme site. When the solution settled, the excess salt collected at the bottom of the vial. The excess salt was filtered off using a glass pipette with a small piece of glass microfiber filter paper at the bottom of the pipette, which let the solution containing the product pass through and collected the excess salt on top of the glass microfiber filter paper that is inside the pipette. The solution was transferred to a Schlenk flask charged with a stir bar. The solution was then reacted with excess NO gas on the Schlenk line. The reaction was allowed to stir 30 - 60 min in the glovebox. For the control complexes, [Zn(TPP)-trz-Fe(BMPA-Pr)(NO)](BF4) and [Fe(TPP)(NO)-trz-(BMPA-Pr)], the nitrosylated solutions were layered with hexanes to allow the complexes to precipitate in the glovebox freezer overnight. The next day the NO in the headspace was purged and the precipitated solid was filtered off in the glove box. For the rest of the complexes, excess NO was removed from the headspace of the Schlenk flasks by purging with N_2 gas for \sim 10 min. Attempts to precipitate the nitrosylated complexes were unsuccessful, so the solutions were analyzed instead. The concentrations of the complexes were adjusted to the desired concentration for each characterization technique (solution IR (5 - 10 mM), EPR (1 mM), and UV-Vis spectroscopy (\sim 3 μ M). N_2 O production was tested for as described above.

For the complex [Fe^{II}(TPP)-trz-Fe^{II}(BMPA-Pr)](BF₄), the oxidation state of the non-heme iron center after reaction with NO gas was probed by a ferrocenium assay. The disappearance of the absorption band of [FeCp₂](PF₆) was tracked by UV-Vis spectroscopy as the ferrocenium salt was titrated with the nitrosylated clicked complex. If the absorption band at 621 nm of ferrocenium persists, then this would indicate that the oxidation state of the non-heme iron is Fe^{III}, but if it disappears it would indicate the Fe^{II} oxidation state.

For [Fe(TPP)-trz-Fe(TMPA)](OTf)₂ and [Fe(TPP)-trz-Fe(BMPA-PhO)](OTf) where dinitrosyl formation was observed, CoCp₂ was added to the solution which was then characterized using solution IR spectroscopy. Gas headspace analysis was used to probe for N₂O production. The further characterization of the nitrosylated clicked complexes is described in the Results & Analysis section.

3. Results & Analysis

Synthesis of Clicked Complexes.

Three new clicked complexes have been synthesized as shown in Figure 3. Click chemistry allows for a modular synthesis of these complexes, where the heme and non-heme units can be synthesized independently (and in parallel), resulting in a quicker and higher yielding synthetic pathway. This synthetic approach also lends itself to exchanging the metal centers selectively to explore specific questions about the heme and non-heme sites.

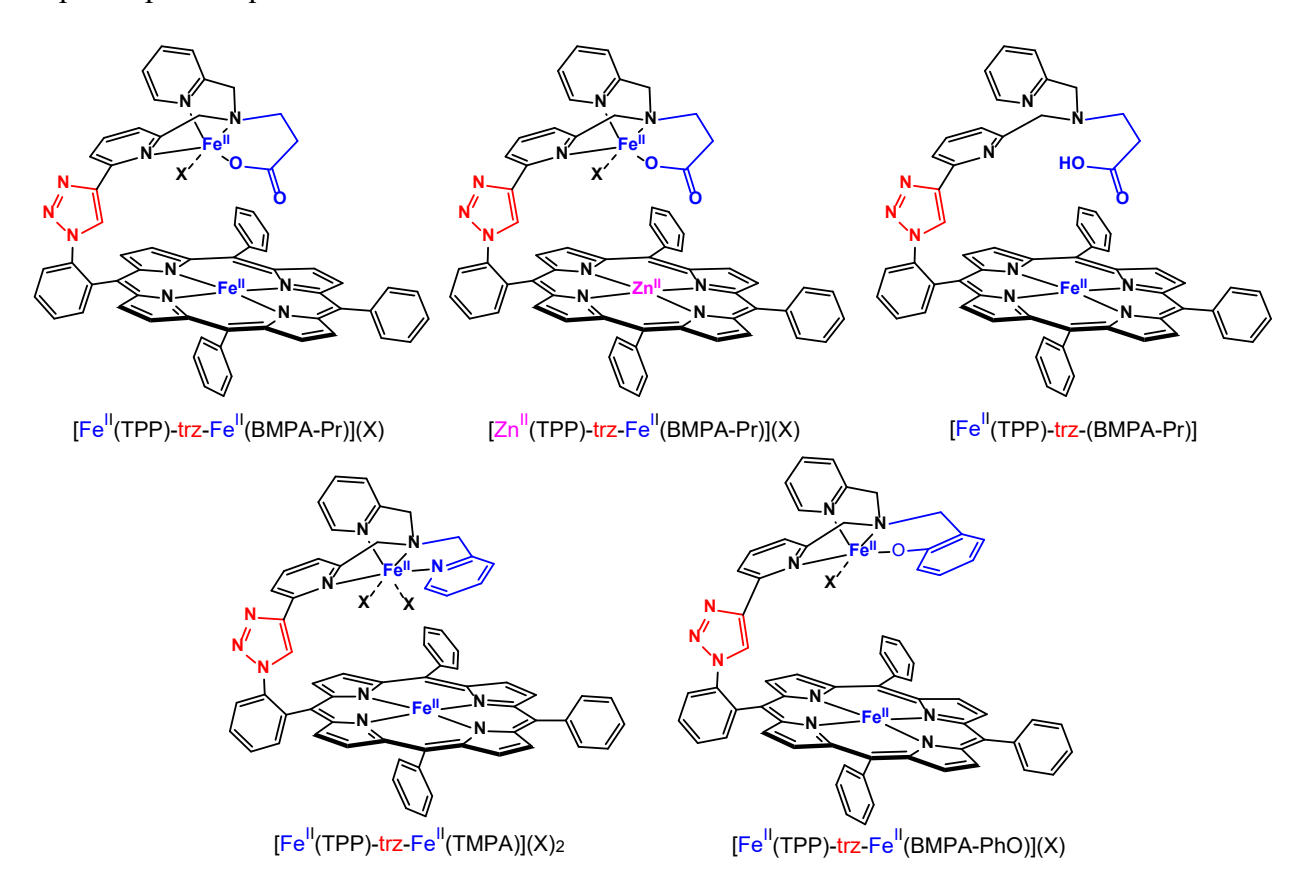
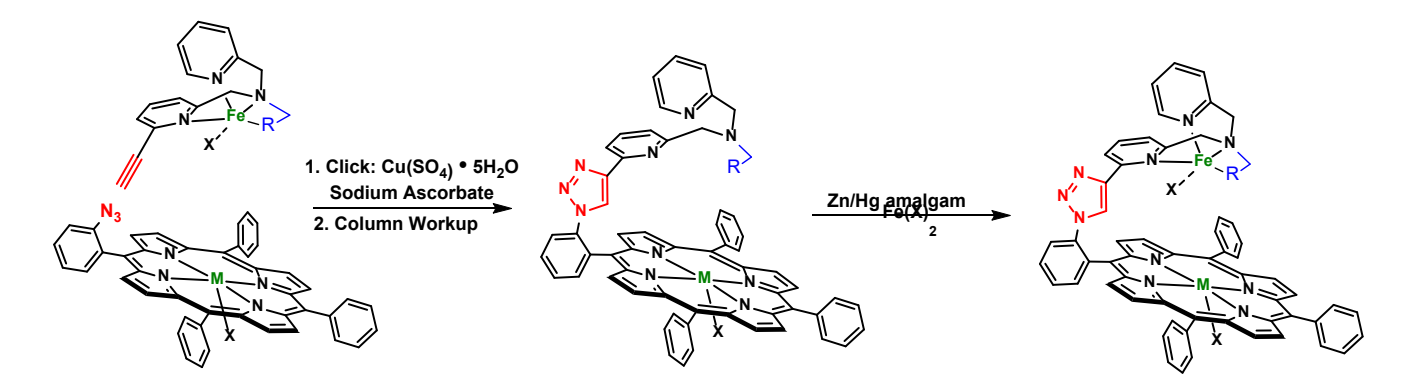


Figure 3. Synthetic click complexes studied in this work ($X = BF_4^-$ or OTf^-).

A general scheme for the synthesis of these complexes is shown in Scheme 1. Here, the heme b_3 in the NorBC active site is mimicked by a modified tetraphenylporphyrin (H₂[TPP]) ligand with

a mono-azide group on one of the phenyl rings (the synthesis of H₂[m-N₃TPP] is documented in the Experimental Section and the characterization data – CV, EPR, and ¹H-NMR spectroscopy – can be found in the Supplemental Information). The Fe_B site of NorBC is mimicked using modified bis(methylpyridyl)amine (BMPA) ligand scaffolds with an alkyne group on the 2-position of one of the pyridine groups. Three different variations of the non-heme ligand were explored as shown in Figure 3 (the syntheses of the non-heme alkyne precursors are provided in the Experimental Section and the characterization data – CV, EPR, and ¹H-NMR spectroscopy – can be found in the Supplemental Information). The heme and non-heme precursor complexes are fused using an azide-alkyne cycloaddition (the famous "click" reaction), resulting in the triazole-linked, clicked complex. Both of the heme and non-heme precursor complexes are metallated before the click reaction is performed to prevent unwanted binding of the copper catalyst employed for the click reaction. Upon column workup, the metal in the non-heme site is removed. This allows for the remetallation of the non-heme site with any desired metal of interest.



Scheme 1. General scheme of the click reaction between the alkyne and azide functionalized precursors to form the clicked triazole-linked complex ($X = Cl^-$, BF_{4^-} , OTf^- ; M = Zn, Fe; and R = pyridine, propionate, or phenolate functional groups).

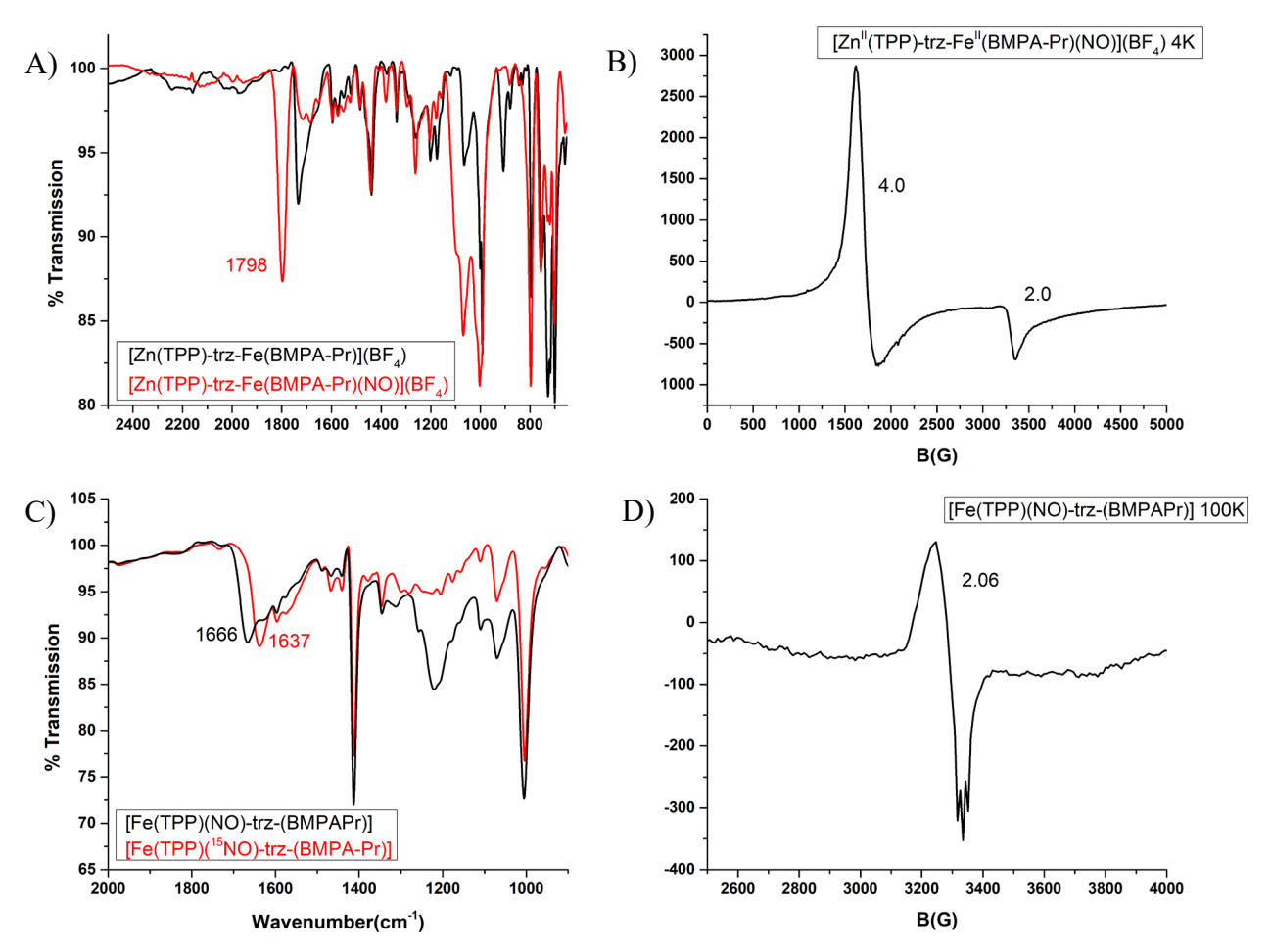
Due to the presence of the carboxylate arm in [Fe^{III}(TPP)(Cl)-trz-(BMPA-Pr)], we found that the non-heme site is difficult to metallate when the heme is in the Fe^{III} state. A procedure was

developed where the iron in the heme site is first reduced using Zn/Hg amalgam in order to favor a four-coordinate (4C) Fe^{II}(TPP) unit that would not interact with the carboxylate group of the non-heme site. Then the non-heme site is metallated with the desired metal. In order to assess the spectroscopic signatures of each site independently, two control complexes were prepared and fully characterized.

 $Control\ Complexes:\ [Zn^{II}(TPP)-trz-Fe^{II}(BMPA-Pr)](BF_4)\ and\ [Fe^{II}(TPP)-trz-(BMPA-Pr)]$

The non-heme ligand BMPA-Pr was selected to be investigated in the control complexes, since it most closely mimics the Fe_B site of NorBC. For this purpose, the heme site was loaded with the

Figure 4. Control clicked complex [Zn(TPP)-trz-Fe^{II}(BMPA-Pr)(NO)](BF₄) for spectroscopic characterization of the non-heme iron center. (A) IR and (B) EPR spectra showing the formation



of a non-heme hs-{FeNO}⁷ complex upon reaction of the Zn(II)/Fe(II) precursor with NO gas. Control clicked complex [Fe^{II}(TPP)(NO)-trz-(BMPA-Pr)] for spectroscopic characterization of the heme center. (C) IR and (D) EPR spectra showing the formation of a heme ls-{FeNO}⁷ complex.

diamagnetic metal zinc and the non-heme site was loaded with iron, to yield [Zn^{II}(TPP)-trz-Fe^{II}(BMPA-Pr)](BF₄). This complex was then reacted with excess NO gas, and subsequently characterized by IR and EPR spectroscopy. [Zn^{II}(TPP)-trz-Fe^{II}(BMPA-Pr)(NO)](BF₄) exhibits an

N-O stretching frequency of 1798 cm⁻¹, which is in the expected range for a non-heme hs-{FeNO}⁷ complex (see Figure 4 top). Porphyrins have absorption bands in the UV-Vis spectral range with significantly higher extinction coefficients compared to non-heme iron complexes, so the UV-Vis spectrum is dominated by the spectroscopic signatures of the heme subunit. Thus, the UV-Vis spectrum of [Zn^{II}(TPP)-trz-Fe^{II}(BMPA-Pr)](BF₄) is unperturbed upon nitrosylation, showing peaks at 420 and 550 nm. The EPR spectrum of the nitrosylated complex at 4 K has signals at effective g-values of 4.0, 2.0, confirming the expected nitrosylated non-heme hs-{FeNO}⁷ complex. No N₂O was observed, indicating that a stable nitrosyl complex is formed. The second control complex, [Fe^{II}(TPP)(NO)-trz-(BMPA-Pr)], shows an N-O stretching frequency of 1666 cm⁻¹ after nitrosylation, corresponding to a five-coordinate (5C) ferrous heme-nitrosyl complex (Figure 4).⁷² The EPR and UV-Vis spectra confirm this finding. In particular, the EPR spectrum shows a signal at a g-value of 2.0 with a characteristic three-line hyperfine splitting, arising from the nitrogen atom of the coordinated NO ligand. The UV-Vis spectrum shows the Soret band at 408 nm, typical for 5C ferrous heme-nitrosyls. N₂O formation was not observed. With the control complexes characterized, the diiron complex was generated and the NO reactivity was investigated.

NO Reactivity of $[Fe^{II}(TPP)-trz-Fe^{II}(BMPA-Pr)](BF_4)$.

[Fe^{II}(TPP)-trz-Fe^{II}(BMPA-Pr)](BF₄) was prepared by reducing [Fe^{III}(TPP)(C1)-trz-(BMPA-Pr)] in the glovebox with Zn/Hg amalgam to the corresponding ferrous heme complex, followed by stirring the resulting compound with excess [Fe(BF₄)₂]·2.5CH₃CN to metallate the non-heme site. The resulting solution was then filtered to give [Fe^{II}(TPP)-trz-Fe^{II}(BMPA-Pr)](BF₄). The reduced diiron clicked complex was subsequently reacted with excess NO gas and further characterized

(Figure 5). Attempts to precipitate the nitrosylated complex with various solvents were unsuccessful, so all spectroscopic analysis was performed in the solution state. The reduced complex has a "split" Soret band at 417/443 nm. Some metalloporphyrins exhibit what is known as a split Soret band, in which the Soret band is split into two components, arising from the interaction between the porphyrin Soret ($\pi \rightarrow \pi^*$) excited state and charge transfer excited states involving the metal ion (in this case iron).⁷³⁻⁷⁸ [Fe^{II}(TPP)-trz-Fe^{II}(BMPA-Pr)(BF₄) has a split Soret band, which is not unusual for reduced 4C iron porphyrins. UV-Vis spectroscopy showed a shift in the Soret band from 417/443 nm to 408 nm upon NO addition, as shown in Figure 5A,

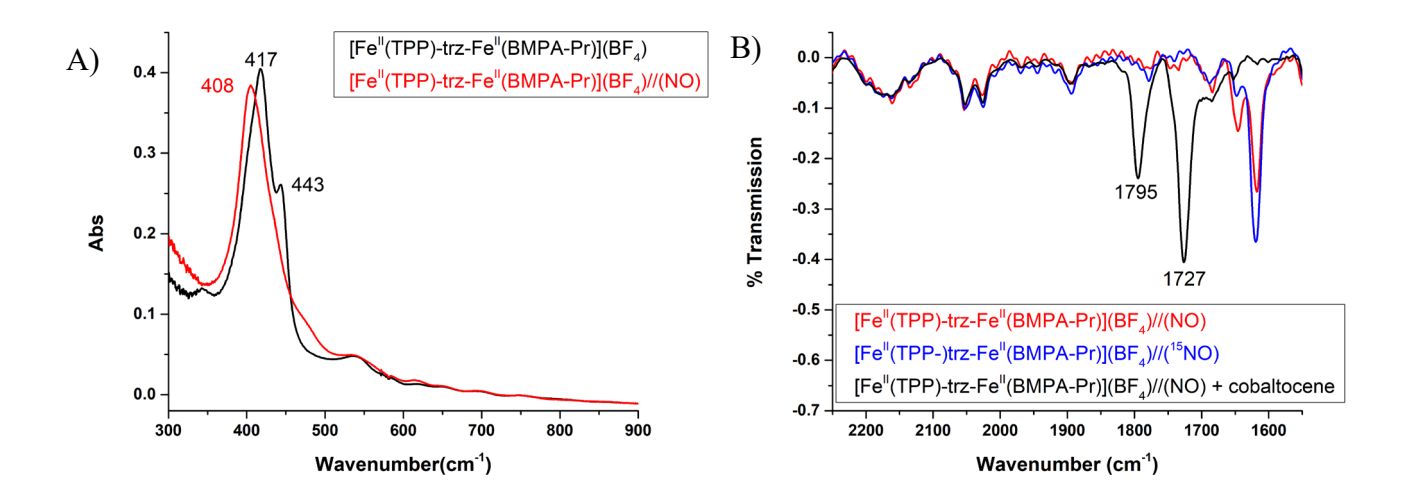


Figure 5. (A) UV-Vis spectrum of [Fe^{II}(TPP)-trz-Fe^{II}(BMPA-Pr)](BF₄) (fully reduced) overlayed with the spectrum of the complex after reaction with NO. (B) Overlay of the IR spectra of [Fe^{II}(TPP)-trz-Fe^{II}(BMPA-Pr)](BF₄)//NO (reacted with NO; red) and ¹⁵NO (blue), and [Fe^{II}(TPP)-trz-Fe^{II}(BMPA-Pr)](BF₄)//NO after the addition of excess cobaltocene (black).

indicating that the heme has reacted upon addition of NO. This shift in the Soret band indicates that NO is binding to the porphyrin. Unexpectedly, however, the IR spectrum of the solution did not show any ¹⁵N isotope-sensitive bands in the 1600 - 1800 cm⁻¹ range, indicating that no NO complex has formed, at least not as a major product. EPR spectroscopy revealed the presence of a

small amount of a ferrous heme ls-{FeNO}⁷ complex, which was quantified by comparison to a known standard of [Fe(TPP)(NO)] (1 mM), giving a 20% yield for this species (Figure S9). This complex was not competent towards N₂O formation. Notably, the oxidation state of the non-heme site after nitrosylation remains ferrous, which was confirmed by titrating the oxidant ferrocenium with the nitrosylated clicked complex in solution, and by monitoring the disappearance of the absorption band of ferrocenium at 621 nm (Figure S11). This result implies that for some reason, the non-heme iron center is unable to bind NO in [Fe^{II}(TPP)-trz-Fe^{II}(BMPA-Pr)](BF₄). This is surprising, as ferrous non-heme complexes usually have a high affinity for NO, in contrast to the behavior of the non-heme iron site observed here. This could potentially be due to the presence of the propionate arm that is binding in such a way that it is not allowing NO to access the non-heme iron center. However, upon addition of excess cobaltocene (3 equiv) to the nitrosylated solution of [Fe^{II}(TPP)-trz-Fe^{II}(BMPA-Pr)](BF₄), two new bands appeared in the solution IR spectrum at 1795 and 1727 cm⁻¹, as seen in Figure 5B. These bands are separated by 68 cm⁻¹, which is in the typical range for the N-O stretching frequencies in Dinitrosyl Iron Complexes (DNICs). 44 The vibrational frequencies of the two N-O stretches indicate that this is a {Fe(NO)₂}⁹-type DNIC. In this regard, please note that it has previously been reported that the one-electron reduction of ferrous non-heme iron-NO complexes to the hs-{FeNO}⁸ state leads to the formation of DNICs. ^{68,79,80} This result indicates that the non-heme iron site in [Fe^{II}(TPP)-trz-Fe^{II}(BMPA-Pr)](BF₄) has a very low affinity for NO, and that upon addition of a reductant a more stable DNIC can form in high yield, potentially via a disproportionation reaction (see Discussion). 81 At the same time, the heme site is only partially nitrosylated.

NO Reactivity of $[Fe^{II}(TPP)-trz-Fe^{II}(TMPA)](OTf)_2$ and $[Fe^{II}(TPP)-trz-Fe^{II}(BMPA-PhO)](OTf)$.

[Fe^{II}(TPP)-trz-Fe^{II}(TMPA)](OTf)₂ was prepared in the same manner as [Fe^{II}(TPP)-trz-Fe^{II}(BMPA-Pr)](BF₄), but it is of note that [Fe^{II}(TPP)-trz-Fe^{II}(TMPA)](OTf)₂ could be metallated prior to reduction with no difficulty metallating the non-heme site (the equivalent IR spectra of the nitrosylated complex with the BF₄⁻ counter ion can be found in the SI). Upon reaction with NO, NO was observed to bind to both iron sites forming a stable diiron dinitrosyl complex (Figure 6). The N-O stretching band corresponding to the non-heme hs-{FeNO}⁷ complex is found at 1789 cm⁻¹, whereas the N-O stretch of the heme ls-{FeNO}⁷ complex is located at 1684 cm⁻¹. The broadness of the heme-nitrosyl IR band could be due to NO binding at different faces of the porphyrin. UV-Vis and EPR spectroscopy also confirmed the formation of a diiron dinitrosyl complex (Figure S10), with a shift of the Soret band to 408 nm and effective g-values of 4.0 and 2.0 at 4 K (non-heme iron-nitrosyl) and g = 2.0 with a three-line hyperfine splitting at 100 K (hemenitrosyl). The amount of heme ls-{FeNO}⁷ complex formed was quantified by integrating the EPR spectrum at 100 K, showing that this species forms at about 80% yield (Figure S14). With the formation of a diiron dinitrosyl complex, the semi-reduction pathway⁶⁸ was explored by adding 1 equiv of cobaltocene to a solution of the complex, and testing if N2O was formed. N2O was not detected, but instead, the formation of a DNIC was observed with bands at 1782 cm⁻¹ and 1710 cm⁻¹ as seen in Figure 6B, again corresponding to a {Fe(NO)₂}⁹ complex. It is possible that the NO ligand is binding on the proximal side of the heme, so it is unable to couple with the non-heme iron-bound NO to form N₂O, ultimately leading to dead-end DNIC formation. Similar issues have been previously reported in the literature. 47,59 In the Lu group's Fe_BMb model, it was found that NO could displace the proximal histidine and lead to a dead-end product that could not form N₂O.

A peripheral glutamate residue was added to keep the histidine from being displaced and enforcing NO binding on the distal side, which led to a catalytically active model. ⁵⁹ Similary, the Karlin group's synthetic model complex, where a partially fluorinated tetraphenylporphyrin is tethered to a tetradentate TMPA ligand, was found to bind NO on the proximal side of the heme, which prevents it from interacting with the NO bound to the Fe_B site mimic, leading to a complex that is not active for NO reduction. ⁴⁷ [Fe^{II}(TPP)-trz-Fe^{II}(TMPA)](OTf)₂ lacks the carboxylate arm and is able to form a stable diiron dinitrosyl complex, suggesting that the carboxylate arm in [Fe^{II}(TPP)-trz-Fe^{II}(BMPA-Pr)](BF₄) somehow plays an interfering role, lowering the affinity of the ferrous non-heme iron center in this complex for NO.

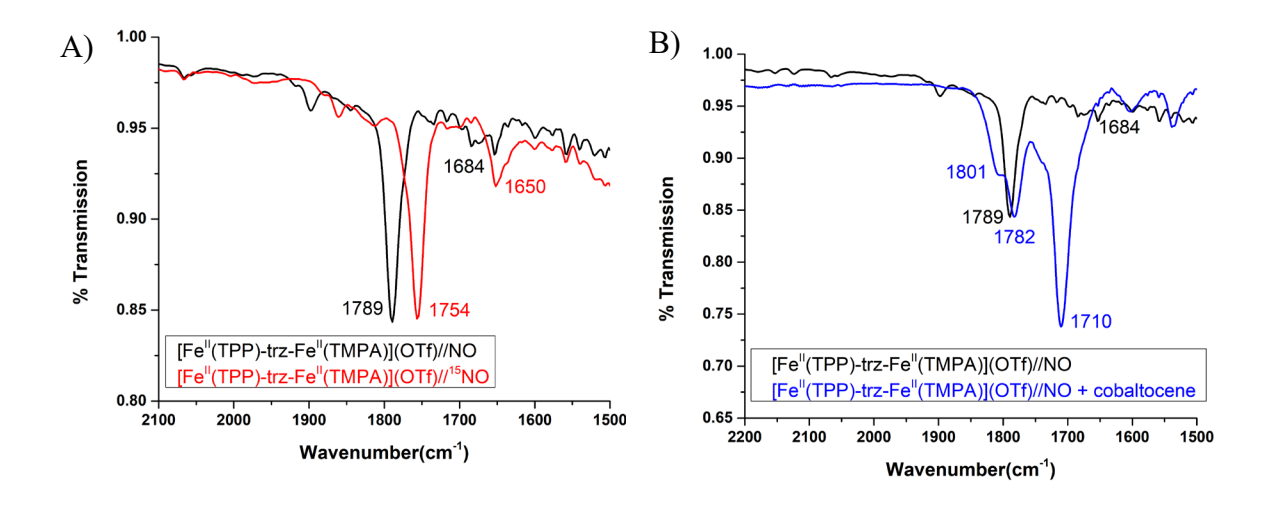


Figure 6. (A) Overlay of the IR spectra of [Fe^{II}(TPP)-trz-Fe^{II}(TMPA)](OTf)₂ after reaction with NO (black) and ¹⁵NO (red). (B) Overlay of the IR spectra of [Fe^{II}(TPP)-trz-Fe^{II}(TMPA)](OTf)₂ with NO (black) and with the addition of 1 equiv of cobaltocene (blue).

[Fe^{II}(TPP)-trz-Fe^{II}(BMPA-PhO)](OTf) was synthesized to test if catalytic activity could be observed if one of the pyridine arms in TMPA was replaced with a phenolate group, which more closely mimics the Glu residue in NorBC. [Fe^{II}(TPP)-trz-Fe^{II}(BMPA-PhO)](OTf), when

nitrosylated, does form a diiron dinitrosyl complex, as observed for [Fe(TPP)-trz-Fe(TMPA)](OTf)₂. The N-O stretching bands of nitrosylated [Fe^{II}(TPP)-trz-Fe^{II}(BMPA-PhO)](BF₄) are observed at 1789 cm⁻¹ (non-heme iron-nitrosyl) and 1684 cm⁻¹ (heme-nitrosyl) (Figure 7A). A total of 75% heme-nitrosyl was formed according to a quantification of the EPR spectrum (Figure S14). Upon addition of 1 equiv of cobaltocene to nitrosylated [Fe^{II}(TPP)-trz-Fe^{II}(BMPA-PhO)](OTf), a DNIC complex was again observed, with N-O stretching frequencies of 1816 and 1740 cm⁻¹ (Figure 7B).

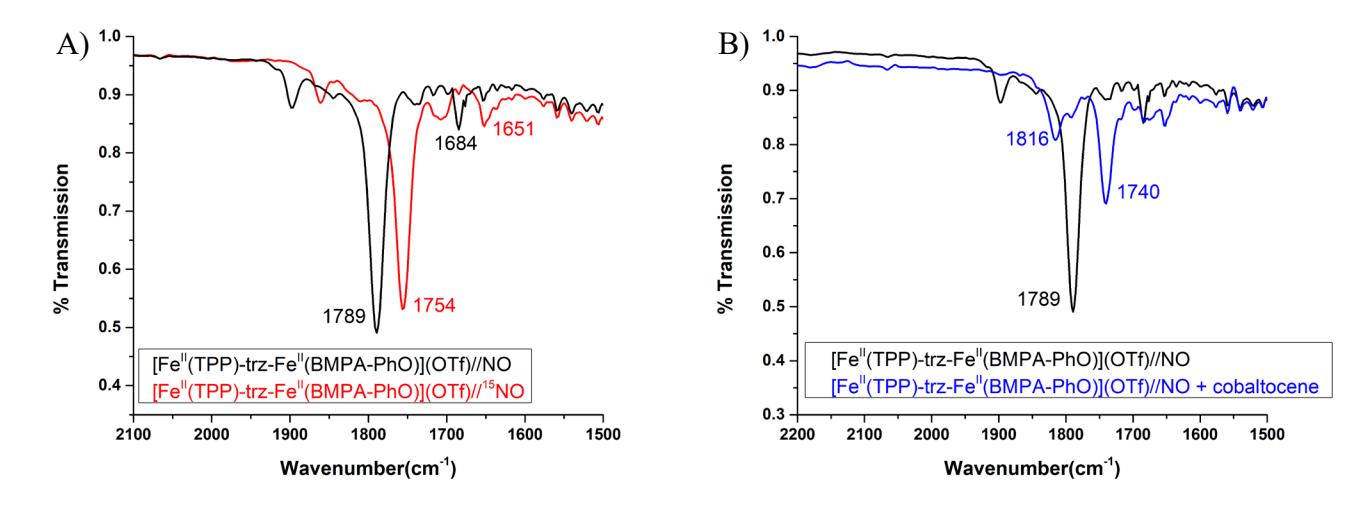


Figure 7. (A) Overlay of the IR spectra of [Fe^{II}(TPP)-trz-Fe^{II}(BMPA-PhO)](OTf) after reaction with NO (black) and ¹⁵NO (red). (B) Overlay of the IR spectra of [Fe^{II}(TPP)-trz-Fe^{II}(BMPA-PhO)](OTf) with NO (black) and with the addition of 1 equiv of cobaltocene (blue).

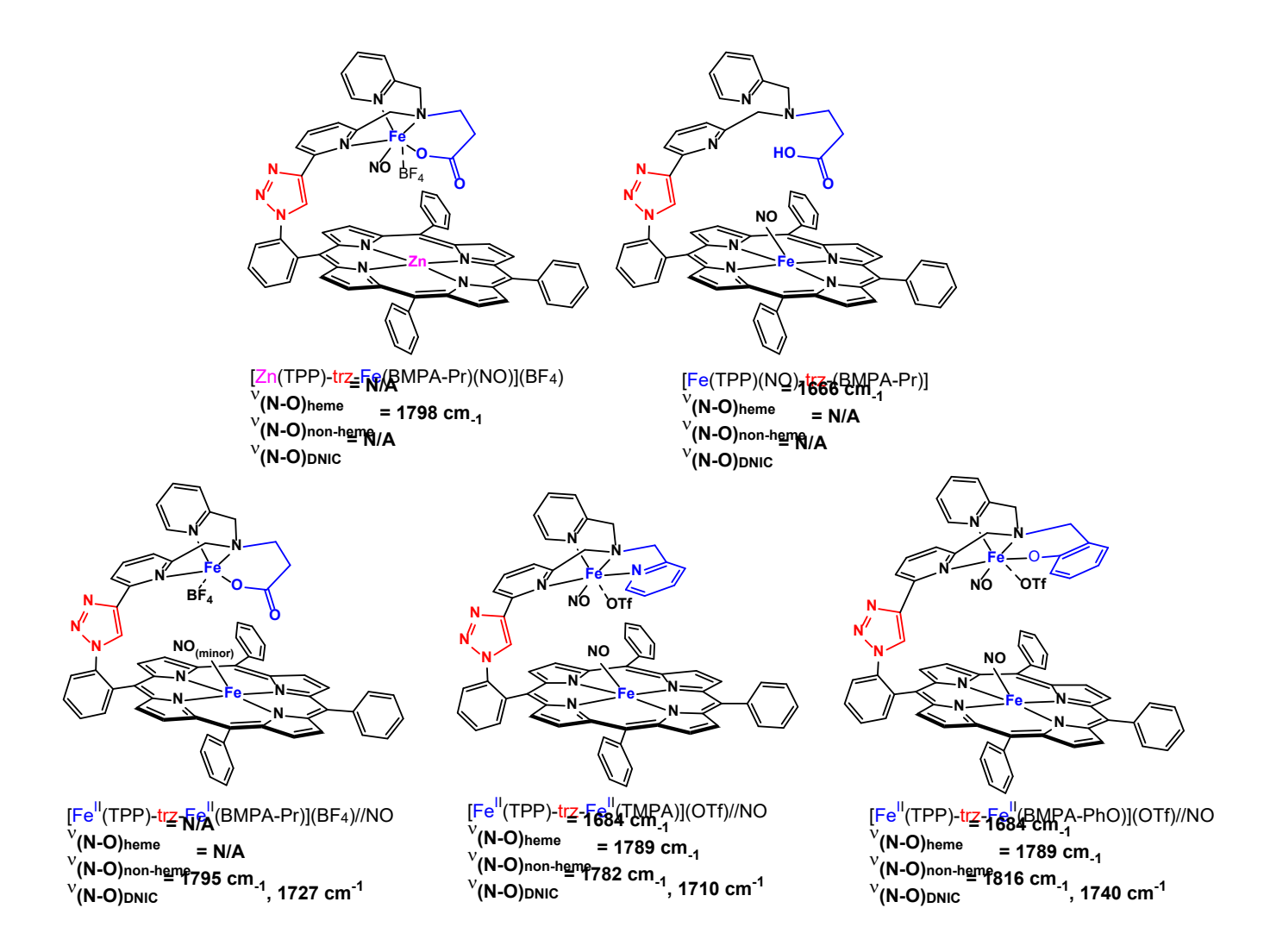


Figure 8. Summary of vibrational data for all of the complexes, including the N-O stretching frequencies obtained by IR spectroscopy for the heme-nitrosyl, non-heme nitrosyl, and DNIC species.

4. Discussion

In this paper, we present a new type of heme/non-heme diiron model complex, assembled using click chemistry, that models the diiron active site of NorBC. This innovative synthetic approach allows a variety of non-heme ligands to be appended to the heme mimic via click chemistry, and it enables the use of different metals in the heme and non-heme ligands in a straightforward way, to explore reactivity. The [Fe(TPP)-trz-Fe(BMPA-Pr)](BF4) scaffold was first investigated for

reactivity with NO as it most closely models the active site of NorBC. [Fe(TPP)-trz-Fe(TMPA)](OTf)₂ was then studied to determine if the carboxylate functional group was playing a role in the lack of NO reactivity at the non-heme iron site of [Fe(TPP)-trz-Fe(BMPA-Pr)](BF₄). Finally, [Fe(TPP)-trz-Fe(BMPA-PhO)](OTf) was synthesized to restore the oxygen coordination at the non-heme site, without the inference from the carboxylate arm.

In order to study the reaction of [Fe^{II}(TPP)-trz-Fe^{II}(BMPA-Pr)](BF₄) with NO, we first investigated the control complexes [Fe^{II}(TPP)-trz-(BMPA-Pr)] and [Zn^{II}(TPP)-trz-Fe^{II}(BMPA-Pr)](BF₄). These compounds form stable nitrosyl complexes that were further characterized using UV-Vis, IR and EPR spectroscopy. Unlike the control complexes, when the clicked complex is fully loaded with iron, [Fe^{II}(TPP)-trz-Fe^{II}(BMPA-Pr)](BF₄), and reacted with NO it surprisingly only formed a minor amount of nitrosylated complex (according to UV-Vis and EPR spectroscopy): a small amount (20%) of heme ls-{FeNO}⁷ complex was formed, whereas the nonheme site seemed largely unreactive towards NO. In the case of the heme component, we posit that the majority is oxidized to the ferric state, based on the UV-Vis data. Surprisingly, the nonheme iron remains ferrous, which was shown by a titration of the oxidant [Fe(Cp₂)](PF₆) with the nitrosylated clicked complex in solution. However, upon addition of cobaltocene to a solution of nitrosylated [Fe^{II}(TPP)-trz-Fe^{II}(BMPA-Pr)](BF₄), DNIC formation was observed. As previously determined, one-electron reduction of ferrous non-heme hs-{FeNO}⁷ complexes leads to the formation of DNICs through disproportionation of the resulting hs-{FeNO}⁸ complex.⁴⁴ In the reaction of nitrosylated [Fe^{II}(TPP)-trz-Fe^{II}(BMPA-Pr)](BF₄) with CoCp₂, a {Fe(NO)₂} DNIC is formed. Two possible mechanistic scenarios are: (a) the reaction of a reduced hs-{FeNO}⁸ with a hs-{FeNO}⁷ complex, according to:

$$hs-{FeNO}^7 + hs-{FeNO}^8 \rightarrow {Fe(NO)_2}^9 + "Fe^{II"}$$

or, (b) since the nitrosylated complex was not isolated and the solution likely contained some dissolved NO, this excess NO could be the source of the second equivalent of NO:

$$hs-\{FeNO\}^8 + NO(g) \rightarrow \{Fe(NO)_2\}^9$$

to form the DNIC. EPR spectra, determined at 100 K after the addition of cobaltocene to the nitrosylated complex, show that the signal at a g-value of 2.0, corresponding to the heme ls-{FeNO}⁷ complex, was still present. This implies that the non-heme iron center in [Fe^{II}(TPP)-trz-Fe^{II}(BMPA-Pr)](BF₄) only has a very low affinity for NO, creating only very small amounts of the hs-{FeNO}⁷ complex. After reduction to the hs-{FeNO}⁸ state, formation of the very stable {Fe(NO)₂}⁹ DNIC then allows for its formation in quantitative yield over time, likely via mechanism (b), considering the very small amount of hs-{FeNO}⁷ present in solution.

When the carboxylate arm of the non-heme site is replaced with either a phenolate or pyridine group, the complex is now able to bind NO to both metal sites. A summary of the vibrational data of all of the complexes is shown in Figure 8. This suggests that the carboxylate functional group is causing the non-heme site to be unreactive towards NO in [Fe^{II}(TPP)-trz-Fe^{II}(BMPA-Pr)](BF₄). Interestingly, [Fe^{II}(TPP)-trz-Fe^{II}(TMPA)](OTf)₂ and [Fe^{II}(TPP)-trz-Fe^{II}(BMPA-PhO)](OTf), after reaction with NO, show the same N-O stretching frequency of 1789 cm⁻¹ for the non-heme hs-{FeNO}⁷ component. This suggests that one of the pyridine groups in [Fe^{II}(TPP)-trz-Fe^{II}(BMPA-PhO)](OTf) are not bound to the non-heme iron site in the respective NO complexes. Hence, the resulting hs-{FeNO}⁷ complexes both have either N₃X(NO) or N₃X₂(NO) coordination environments, where X is a counter ion or solvent molecule. A difference in the coordination environments of the hs-{FeNO}⁷ complexes would lead to a difference in their N-O stretches, as the N-O stretching frequency is very sensitive to the exact coordination sphere of the iron centers.^{82,83} This could

mean that the phenolate functional group in [Fe^{II}(TPP)-trz-Fe^{II}(BMPA-PhO)](OTf) is too sterically hindered to bind. The phenolate functional group was selected to more closely mimic the Glu in the active site of NorBC, which would hopefully aid in catalytic activity. If the phenolate group is not binding to the non-heme iron center, then increasing the chain length of the phenolate arm attached to the BMPA base would potentially allow for the flexibility needed for the phenolate group to coordinate the non-heme iron center.

While our new synthetic approach utilizing click chemistry allowed for a more efficient and higher yielding synthesis of linked heme/non-heme iron model complexes, the triazole linker does not seem to facilitate interaction of the two iron sites to allow the complexes to be catalytically active for NO reduction. In other words, the heme and non-heme iron sites are not in the proper orientation for metal-metal cooperativity and bimetallic activation of NO. Correspondingly, the three clicked complexes studied here do not produce N₂O. Further support for the idea that the two sites are not interacting comes from analysis of the ¹H-NMR spectra of [Fe^{II}(TPP)-trz-(BMPA-Pr)], [Fe^{II}(TPP)-trz-(BMPA-PhO)], and [Fe^{II}(TPP)-trz-(TMPA)] (Figure S8-S10). The Karlin group analyzed the complex [Fe^{II}(F₈TPP)/(TMPA)] (named (⁶L)Fe^{II}) by deuteration experiments to assign the ¹H-NMR spectrum of this complex. ⁸⁴ They found that the pyridyl arm weakly coordinates to the porphyrin iron center and this is evident from changes in the shifts of the pyrrolic H atoms. When there is weak coordination, the signal of the pyrrole H atoms splits from a singlet at around 4.9 ppm in CH₂Cl₂ into four peaks and shifts into the 40-60 ppm region, due to the Fe^{II} center being in the S=2 state. In the ¹H-NMR spectra of our complexes there are no signals present in the 40-60 ppm region, indicating that the non-heme ligand is not interacting with the porphyrin site, and instead, the ferrous porphyrin is four-coordinate and in the S=1 state. When a dinitrosyl was formed in the case of [Fe^{II}(TPP)-trz-Fe^{II}(TMPA)](OTf)₂ and [Fe^{II}(TPP)-trz-Fe^{II}(BMPA-

PhO)](OTf), addition of cobaltocene did not lead to N-N coupling and N₂O formation, following the semireduced pathway.⁶⁷ Instead, DNIC formation was observed. In order to promote catalytic activity, the complexes need to be redesigned to promote NO binding in an orientation that mediates N-N coupling. This work is in progress.

Corresponding Author

<u>lehnertn@umich.edu</u>

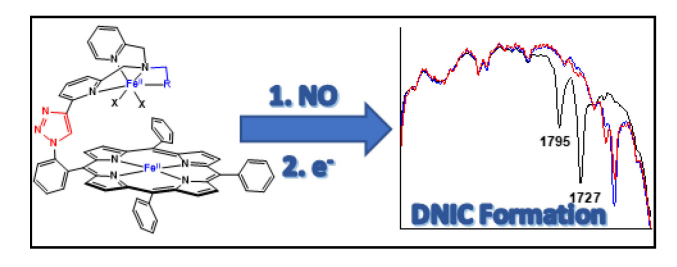
ORCID:

Nicolai Lehnert: 0000-0002-5221-5498 Jill Harland: 0000-0003-0274-6722

Declaration of Competing Interest: The authors declare that they have no known competing financial interests or personal relationships that could have appeared to influence the work reported in this paper.

Acknowledgment: This work was supported by the National Science Foundation (CHE-2002885 to NL). JBH acknowledges support from a Robert W. Parry Scholarship and a Milton Tamres Teaching Award (both University of Michigan).

TOC Figure:



References.

- 1. Canfield, D. E.; Glazer, A. N.; Falkowski, P. G. The Evolution and Future of Earth's Nitrogen Cycle. *Science* **2010**, *330*, 192-196.
- 2. Galloway, J. N.; Townsend, A. R.; Erisman, J. W.; Bekunda, M.; Cai, Z.; Freney, J. R.; Martinelli, L. A.; Seitzinger, S. P.; Sutton, M. A. Transformation of the Nitrogen Cycle: Recent Trends, Questions, and Potential Solutions. *Science* **2008**, *320*, 889-892.
- 3. Lehnert, N.; Dong, H. T.; Harland, J. B.; Hunt, A. P.; White, C. J. Reversing Nitrogen Fixation. *Nat. Rev. Chem.* **2018**, *2*, 278-289.
- 4. Lehnert, N.; Kim, E.; Dong, H. T.; Harland, J. B.; Hunt, A. P.; Manickas, E. C.; Oakley, K. M.; Pham, J.; Reed, G. C.; Sosa Alfaro, V. The Biologically Relevant Coordination Chemistry of Iron and Nitric Oxide: Electronic Structure and Reactivity. *Chem. Rev.* **2021**, *121*, 14682-14905.
- 5. Lehnert, N.; Coruzzi, G.; Hegg, E.; Seefeldt, L.; Stein, L. Feeding the world in the 21st century: grand challenges in the nitrogen cycle. *NSF: Arlington, VA, USA* **2015**.
- 6. Erisman, J. W.; Sutton, M. A.; Galloway, J.; Klimont, Z.; Winiwarter, W. How a century of ammonia synthesis changed the world. *Nat. Geosci.* **2008**, *1*, 636-639.
- 7. Godfray, H. C.; Beddington, J. R.; Crute, I. R.; Haddad, L.; Lawrence, D.; Muir, J. F.; Pretty, J.; Robinson, S.; Thomas, S. M.; Toulmin, C. Food security: the challenge of feeding 9 billion people. *Science* **2010**, *327*, 812-818.
- 8. Smil, V. Enriching the Earth: Fritz Haber, Carl Bosch and the Transformation of World Food Production.; MIT Press: Cambridge, 2001.
- 9. Ferguson, S. J. Nitrogen Cycle Enzymology. Curr. Opin. Chem. Biol. 1998, 2, 182-193.
- 10. Kuypers, M. M.; Marchant, H. K.; Kartal, B. The microbial nitrogen-cycling network. *Nat. Rev. Microbiol.* **2018**, *16*, 263-276.
- 11. Maia, L. B.; Moura, J. J. G. How Biology Handles Nitrite. *Chem. Rev.* **2014**, *114*, 5273-5357.
- 12. Richardson, D. J.; Watmough, N. J. Inorganic Nitrogen Metabolism in Bacteria. *Curr. Opin. Chem. Biol.* **1999**, *3*, 207-219.
- 13. Hooper, A. B.; Vannelli, T.; Bergmann, D. J.; Arciero, D. M. Enzymology of the oxidation of ammonia to nitrite by bacteria. *Antonie van Leeuwenhoek* **1997**, *71*, 59-67.
- 14. Kozlowski, J. A.; Kits, K. D.; Stein, L. Y. Comparison of nitrogen oxide metabolism among diverse ammonia-oxidizing bacteria. *Front. Microbiol.* **2016**, *7*, 1090.
- 15. Winogradsky, S. On the nitrifying organisms. *Sciences* **1890**, *110*, 1013-1016.
- 16. Francis, C. A.; Beman, J. M.; Kuypers, M. M. M. New processes and players in the nitrogen cycle: the microbial ecology of anaerobic and archaeal ammonia oxidation. *ISME J.* **2007**, *1*, 19-27.
- 17. Könneke, M.; Bernhard, A. E.; José, R.; Walker, C. B.; Waterbury, J. B.; Stahl, D. A. Isolation of an autotrophic ammonia-oxidizing marine archaeon. *Nature* **2005**, *437*, 543-546.
- 18. Kozlowski, J. A.; Stieglmeier, M.; Schleper, C.; Klotz, M. G.; Stein, L. Y. Pathways and key intermediates required for obligate aerobic ammonia-dependent chemolithotrophy in bacteria and Thaumarchaeota. *ISME J.* **2016**, *10*, 1836-1845.
- 19. Ferousi, C.; Majer, S. H.; DiMucci, I. M.; Lancaster, K. M. Biological and Bioinspired Inorganic N–N Bond-Forming Reactions. *Chem. Rev.* **2020**, *120*, 5252-5307.

- 20. Hooper, A. B.; Arciero, D.; Bergmann, D.; Hendrich, M. P. In *The Oxidation of Ammonia* as an Engergy Source in Bacteria; Zannoni, D., Ed.; Springer: Dordrecht, Netherlands, 2005; Vol. 16,, p 121-147.
- 21. Daims, H.; Lücker, S.; Wagner, M. A new perspective on microbes formerly known as nitrite-oxidizing bacteria. *Trends Microbiol.* **2016**, *24*, 699-712.
- 22. Winogradsky, S. Contributions a la morphologie des organisms de la nitrification. *Arch. Sci. Biol. (St. Petersbourg)* **1892**, *1*, 87-137.
- 23. Daims, H.; Lebedeva, E. V.; Pjevac, P.; Han, P.; Herbold, C.; Albertsen, M.; Jehmlich, N.; Palatinszky, M.; Vierheilig, J.; Bulaev, A. Complete nitrification by Nitrospira bacteria. *Nature* **2015**, *528*, 504-509.
- 24. Van Kessel, M. A. H. J.; Speth, D. R.; Albertsen, M.; Nielsen, P. H.; Op den Camp, H. J. M.; Kartal, B.; Jetten, M. S. M.; Lücker, S. Complete nitrification by a single microorganism. *Nature* **2015**, *528*, 555-559.
- 25. Galloway, J. N.; Leach, A. M.; Bleeker, A.; Erisman, J. W. A chronology of human understanding of the nitrogen cycle. *Philos. Trans. R. Soc. Lond. B Biol. Sci.* **2013**, *368*, 20130120.
- 26. Moura, I.; Moura, J. J. G. Structural Aspects of Denitrifying Enzymes. *Curr. Opin. Chem. Biol.* **2001**, *5*, 168-175.
- 27. Zumft, W. G. Cell biology and molecular basis of denitrification. *Microbiol. Mol. Biol. Rev.* **1997**, *61*, 533-616.
- 28. https://www.epa.gov/ghgemissions/overview-greenhouse-gases; Vol. 2021.
- 29. Sousa, F. L.; Alves, R. J.; Ribeiro, M. A.; Pereira-Leal, J. B.; Teixeira, M.; Pereira, M. M. The superfamily of heme–copper oxygen reductases: types and evolutionary considerations. *Biochim. Biophys. Acta, Bioenerg.* **2012**, *1817*, 629-637.
- 30. Watmough, N. J.; Field, S. J.; Hughes, R. J. L.; Richardson, D. J. The Bacterial Respiratory Nitric Oxide Reductase. *Biochem. Soc. Trans.* **2009**, *37*, 392-399.
- 31. Wasser, I. M.; de Vries, S.; Moënne-Loccoz, P.; Schröder, I.; Karlin, K. D. Nitric Oxide in Biological Denitrification: Fe/Cu Metalloenzymes and Metal Complex NO_x Redox Chemistry. *Chem. Rev.* **2002**, *102*, 1201-1234.
- 32. Butland, G.; Spiro, S.; Watmough, N. J.; Richardson, D. J. Two Conserved Glutamates in the Bacterial Nitric Oxide Reductase Are Essential for Activity but Not Assembly of the Enzyme. *J. Bacteriol.* **2001**, *183*, 189-199.
- 33. Cheesman, M. R.; Zumft, W. G.; Thomson, A. J. The MCD and EPR of the Heme Centers of Nitric Oxide Reductase from *Pseudomonas stutzeri*: Evidence That the Enzyme Is Structurally Related to the Heme-Copper Oxidases. *Biochemistry* **1998**, *37*, 3994-4000.
- 34. Hino, T.; Matsumoto, Y.; Nagano, S.; Sugimoto, H.; Fukumori, Y.; Murata, T.; Iwata, S.; Shiro, Y. Structural Basis of Biological N₂O Generation by Bacterial Nitric Oxide Reductase. *Science* **2010**, *330*, 1666-1670.
- 35. Crow, A.; Matsuda, Y.; Arata, H.; Oubrie, A. Structure of the membrane-intrinsic nitric oxide reductase from *Roseobacter denitrificans*. *Biochemistry* **2016**, *55*, 3198-3203.
- 36. Girsch, P.; de Vries, S. Purification and initial kinetic and spectroscopic characterization of NO reductase from *Paracoccus denitrificans*. *Biochim. Biophys. Acta* **1997**, *1318*, 202-216.
- 37. Blomberg, M. R. A. Can Reduction of NO to N_2O in Cytochrome c Dependent Nitric Oxide Reductase Proceed through a Trans-Mechanism? *Biochemistry* **2017**, *56*, 120-131.

- 38. Blomberg, M. R. A.; Siegbahn, P. E. M. Mechanism for N₂O Generation in Bacterial Nitric Oxide Reductase: A Quantum Chemical Study. *Biochemistry* **2012**, *51*, 5173-5186.
- 39. Blomberg, L. M.; Blomberg, M. R. A.; Siegbahn, P. E. M. Reduction of nitric oxide in bacterial nitric oxide reductase a theoretical model study. *Biochim. Biophys. Acta* **2006**, *1757*, 240-252.
- 40. Ye, R. W.; Averill, B. A.; Tiedje, J. M. Denitrification: production and consumption of nitric oxide. *Appl. Environ. Microbiol.* **1994**, *60*, 1053-1058.
- 41. Enemark, J. H.; Feltham, R. D. Principles of Structure, Bonding, and Reactivity for Metal Nitrosyl Complexes. *Coord. Chem. Rev.* **1974**, *13*, 339-406.
- 42. Blomberg, M. R. A.; Siegbahn, P. E. M. Improved free energy profile for reduction of NO in cytochrome *c* dependent nitric oxide reductase (*c*NOR). *J. Comp. Chem.* **2016**, *37*, 1810-1818.
- 43. Butler, C. S.; Seward, H. E.; Greenwood, C.; Thomson, A. J. *Fast* Cytochrome b_o from *Escherichia coli* Binds Two Molecules of Nitric Oxide at Cu_B. *Biochemistry* **1997**, *36*, 16259-16266.
- 44. Speelman, A. L.; Zhang, B.; Silakov, A.; Skodje, K. M.; Alp, E. E.; Zhao, J.; Hu, M. Y.; Kim, E.; Krebs, C.; Lehnert, N. Unusual Synthetic Pathway for an {Fe(NO)₂}⁹ Dinitrosyl Iron Complex (DNIC) and Insight into DNIC Electronic Structure via Nuclear Resonance Vibrational Spectroscopy. *Inorg. Chem.* **2016**, *55*, 5485-5501.
- 45. Takeda, H.; Kimura, T.; Nomura, T.; Horitani, M.; Yokota, A.; Matsubayashi, A.; Ishii, S.; Shiro, Y.; Kubo, M.; Tosha, T. Timing of NO Binding and Protonation in the Catalytic Reaction of Bacterial Nitric Oxide Reductase as Established by Time-Resolved Spectroscopy. *Bull. Chem. Soc. Jpn.* **2020**, *93*, 825-833.
- 46. Takeda, H.; Shimba, K.; Horitani, M.; Kimura, T.; Nomura, T.; Kubo, M.; Shiro, Y.; Tosha, T. Trapping of a Mononitrosyl Nonheme Intermediate of Nitric Oxide Reductase by Cryo-Photolysis of Caged Nitric Oxide. *J. Phys. Chem. B* **2023**.
- 47. Wasser, I. M.; Huang, H.; Moënne-Loccoz, P.; Karlin, K. D. Heme/Non-Heme Diiron(II) Complexes and O₂, CO, and NO Adducts as Reduced and Substrate-Bound Models for the Active Site of Bacterial Nitric Oxide Reductase. *J. Am. Chem. Soc.* **2005**, *127*, 3310-3320.
- 48. Wang, J.; Schopfer, M. P.; Puiu, S. C.; Sarjeant, A. A. N.; Karlin, K. D. Reductive Coupling of Nitrogen Monoxide (NO) Facilitated by Heme/Copper Complexes. *Inorg. Chem.* **2010**, *49*, 1404-1419.
- 49. Adam, S. M.; Wijeratne, G. B.; Rogler, P. J.; Diaz, D. E.; Quist, D. A.; Liu, J. J.; Karlin, K. D. Synthetic Fe/Cu complexes: toward understanding heme-copper oxidase structure and function. *Chem. Rev.* **2018**, *118*, 10840-11022.
- 50. Wang, J.; Schopfer, M. P.; Sarjeant, A. A. N.; Karlin, K. D. Heme-copper assembly mediated reductive coupling of nitrogen monoxide. *J. Am. Chem. Soc.* **2009**, *131*, 450-451.
- 51. Collman, J. P.; Dey, A.; Decreau, R. A.; Yang, Y.; Hosseini, A.; Solomon, E. I.; Eberspacher, T. A. Interaction of nitric oxide with a functional model of cytochrome *c* oxidase. *Proc. Natl. Acad. Sci. U.S.A.* **2008**, *105*, 9892-9896.
- 52. Collman, J. P.; Dey, A.; Yang, Y.; Decreau, R. A.; Ohta, T.; Solomon, E. I. Intermediates Involved in the Two Electron Reduction of NO to N₂O by a Functional Synthetic Model of Heme Containing Bacterial NO Reductase. *J. Am. Chem. Soc.* **2008**, *130*, 16498-16499.

- 53. Schopfer, M. P.; Wang, J.; Karlin, K. D. Bioinspired Heme, Heme/Nonheme Diiron, Heme/Copper, and Inorganic NO_x Chemistry: •NO_(g) Oxidation, Peroxynitrite-Metal Chemistry, and •NO_(g) Reductive Coupling. *Inorg. Chem.* **2010**, *49*, 6267–6282.
- 54. Praneeth, V. K. K.; Näther, C.; Peters, G.; Lehnert, N. Spectroscopic Properties and Electronic Structure of Five- and Six-Coordinate Iron(II) Porphyrin NO Complexes: Effect of the Axial N-Donor Ligand *Inorg. Chem.* **2006**, *45*, 2795-2811.
- 55. Berto, T. C.; Speelman, A.; Zheng, S.; Lehnert, N. Mono- and Dinuclear Non-Heme Iron-Nitrosyl Complexes: Models for Key Intermediates in Bacterial Nitric Oxide Reductases. *Coord. Chem. Rev.* **2013**, *257*, 244-259.
- 56. Lehnert, N.; Scheidt, W. R.; Wolf, M. W. Structure and Bonding in Heme–Nitrosyl Complexes and Implications for Biology. *Struct. Bond.* **2014**, *154*, 155-224.
- 57. Collman, J. P.; Boulatov, R.; Sunderland, C. J.; Fu, L. Functional Analogues of Cytochrome *c* Oxidase, Myoglobin, and Hemoglobin. *Chem. Rev.* **2004**, *104*, 561-588.
- 58. Dey, S. G.; Dey, A. NO and O₂ reactivities of synthetic functional models of nitric oxide reductase and cytochrome c oxidase. *Dalt. Trans.* **2011**, *40*, 12633-12647.
- 59. Matsumura, H.; Hayashi, T.; Chakraborty, S.; Lu, Y.; Moënne-Loccoz, P. The Production of Nitrous Oxide by the Heme/Nonheme Diiron Center of Engineered Myoglobins (Fe_BMbs) Proceeds through a *trans*-Iron-Nitrosyl Dimer. *J. Am. Chem. Soc.* **2014**, *136*, 2420-2431.
- 60. Collman, J. P.; Yang, Y.; Dey, A.; Decreau, R. A.; Ghosh, S.; Ohta, T.; Solomon, E. I. A functional nitric oxide reductase model. *Proc. Natl. Acad. Sci. U.S.A.* **2008**, *105*, 15660-15665.
- 61. Reed, C. J.; Lam, Q. N.; Mirts, E. N.; Lu, Y. Molecular understanding of heteronuclear active sites in heme—copper oxidases, nitric oxide reductases, and sulfite reductases through biomimetic modelling. *Chem. Soc. Rev.* **2021**, *50*, 2486-2539.
- 62. Yeung, N.; Lin, Y. W.; Gao, Y. G.; Zhao, X.; Russell, B. S.; Lei, L.; Miner, K. D.; Robinson, H.; Lu, Y. Rational design of a structural and functional nitric oxide reductase. *Nature* **2009**, *462*, 1079-1082.
- 63. Chakraborty, S.; Reed, J.; Ross, M.; Nilges, M. J.; Petrik, I. D.; Ghosh, S.; Hammes-Schiffer, S.; Sage, J. T.; Zhang, Y.; Schulz, C. E. Spectroscopic and computational study of a nonheme iron nitrosyl center in a biosynthetic model of nitric oxide reductase. *Angew. Chem. Int. Ed.* **2014**, *126*, 2449-2453.
- 64. Bhagi-Damodaran, A.; Reed, J. H.; Zhu, Q.; Shi, Y.; Hosseinzadeh, P.; Sandoval, B. A.; Harnden, K. A.; Wang, S.; Sponholtz, M. R.; Mirts, E. N. Heme redox potentials hold the key to reactivity differences between nitric oxide reductase and heme-copper oxidase. *Proc. Natl. Acad. Sci. U.S.A.* **2018**, *115*, 6195-6200.
- 65. Sabuncu, S.; Reed, J. H.; Lu, Y.; Moënne-Loccoz, P. Nitric Oxide Reductase Activity in Heme–Nonheme Binuclear Engineered Myoglobins through a One-Electron Reduction Cycle. *J. Am. Chem. Soc.* **2018**, *140*, 17389-17393.
- 66. Caesar, P. D. 1, 5-Naphthalenedithiol. *Organic Synth.* **2003**, *33*, 47-47.
- 67. White, C. J.; Speelman, A. L.; Kupper, C.; Demeshko, S.; Meyer, F.; Shanahan, J. P.; Alp, E. E.; Hu, M.; Zhao, J.; Lehnert, N. The Semireduced Mechanism for Nitric Oxide Reduction by Non-Heme Diiron Complexes: Modeling Flavodiiron Nitric Oxide Reductases. *J. Am. Chem. Soc.* **2018**, *140*, 2562-2574.
- 68. White, C. J.; Lengel, M. O.; Bracken, A. J.; Kampf, J. W.; Speelman, A. L.; Alp, E. E.; Hu, M. Y.; Zhao, J.; Lehnert, N. Distortion of the [FeNO]₂ Core in Flavodiiron Nitric Oxide Reductase

- Models Inhibits N–N Bond Formation and Promotes Formation of Unusual Dinitrosyl Iron Complexes: Implications for Catalysis and Reactivity. *J. Am. Chem. Soc.* **2022**, *144*, 3804-3820.
- 69. Zheng, S.; Berto, T. C.; Dahl, E. W.; Hoffman, M. B.; Speelman, A. L.; Lehnert, N. The Functional Model Complex [Fe₂(BPMP)(OPr)(NO)₂](BPh₄)₂ Provides Insight into the Mechanism of Flavodiiron NO Reductases. *J. Am. Chem. Soc.* **2013**, *135*, 4902–4905.
- 70. Merkel, M.; Schnieders, D.; Baldeau, S. M.; Krebs, B. Structural Snapshots of a Dynamic Coordination Sphere in Model Complexes for Catechol 1, 2-Dioxygenases. *Euro. J. Inorg. Chem.* **2004**, *2004*, 783-790.
- 71. Yoon, H.; Lim, J. M.; Gee, H.; Lee, C.; Jeong, Y.; Kim, D.; Jang, W. A porphyrin-based molecular tweezer: guest-induced switching of forward and backward photoinduced energy transfer. *J. Am. Chem. Soc.* **2014**, *136*, 1672-1679.
- 72. Goodrich, L. E.; Paulat, F.; Praneeth, V. K. K.; Lehnert, N. Electronic Structure and Reactivity of Heme-Nitrosyls and Its Significance for Nitric Oxide Sensing, Transport, and Catalysis in Biological Systems. *Inorg. Chem.* **2010**, *49*, 6293–6316.
- 73. Egawa, T.; Proshlyakov, D. A.; Miki, H.; Makino, R.; Ogura, T.; Kitagawa, T.; Ishimura, Y. Effects of a thiolate axial ligand on the $\pi \rightarrow \pi^*$ electronic states of oxoferryl porphyrins: A study of the optical and resonance Raman spectra of compounds I and II of chloroperoxidase. *J. Biol. Inorg. Chem.* **2001**, *6*, 46-54.
- 74. Kadish, K. M.; Larson, G.; Lexa, D.; Momenteau, M. Electrochemical and spectral characterization of the reduction steps of μ -oxo-bis (iron tetraphenylporphyrin) dimer in dimethylformamide. *J. Am. Chem. Soc.* **1975**, *97*, 282-288.
- 75. Safo, M. K.; Nesset, M. J. M.; Walker, F. A.; Debrunner, P. G.; Scheidt, W. R. Models of the Cytochromes. Axial Ligand Orientation and Complex Stability in Iron (II) Porphyrinates: The Case of the Noninteracting $d\pi$ Orbitals. *J. Am. Chem. Soc.* **1997**, *119*, 9438-9448.
- 76. Yamaguchi, K.; Morishima, I. Low-valent iron porphyrins. NMR evidence for π -anion-radical character in two-electron-reduced iron (III) meso-or β -pyrrole-substituted porphyrins. *Inorg. Chem.* **1992**, *31*, 3216-3222.
- 77. Paulat, F.; Praneeth, V. K. K.; Näther, C.; Lehnert, N. Quantum Chemistry-Based Analysis of the Vibrational Spectra of Five-Coordinate Metalloporphyrins [M(TPP)CI]. *Inorg. Chem.* **2006**, *45*, 2835-2856.
- 78. Paulat, F.; Lehnert, N. Detailed Assignment of the Magnetic Circular Dichroism and UV-Vis Spectra of Five-Coordinate High-Spin Ferric [Fe(TPP)(CI)]. *Inorg. Chem.* **2008**, *47*, 4963-4976.
- 79. Feig, A. L.; Bautista, M. T.; Lippard, S. J. A Carboxylate-Bridged Non-heme Diiron Dinitrosyl Complex. *Inorg. Chem.* **1996**, *35*, 6892-6898.
- 80. Dong, H. T.; Speelman, A. L.; Kozemchak, C. E.; Sil, D.; Krebs, C.; Lehnert, N. The Fe₂(NO)₂ Diamond Core: A Unique Structural Motif in Non-Heme Iron-NO Chemistry. *Angew. Chem. Int. Ed.* **2019**, *131*, 17859-17863.
- 81. Lehnert, N.; Fujisawa, K.; Camarena, S.; Dong, H. T.; White, C. J. Activation of Non-Heme Iron-Nitrosyl Complexes: Turning up the Heat. *ACS Catal.* **2019**, *9*, 10499-10518.
- 82. Berto, T. C.; Hoffman, M. B.; Murata, Y.; Landenberger, K. B.; Alp, E. E.; Zhao, J.; Lehnert, N. Structural and Electronic Characterization of Non-Heme Fe(II)-Nitrosyls as Biomimetic Models of the Fe_B Center of Bacterial Nitric Oxide Reductase (NorBC). *J. Am. Chem. Soc.* **2011**, *133*, 16714–16717.

- 83. Dong, H. T.; Camarena, S.; Sil, D.; Lengel, M. O.; Zhao, J.; Hu, M. Y.; Alp, E. E.; Krebs, C.; Lehnert, N. What Is the Right Level of Activation of a High-Spin {FeNO}⁷ Complex to Enable Direct N–N Coupling? Mechanistic Insight into Flavodiiron NO Reductases. *J. Am. Chem. Soc* **2022**, *144*, 16395-16409.
- 84. Ghiladi, R. A.; Karlin, K. D. Low-Temperature UV–Visible and NMR Spectroscopic Investigations of O₂ Binding to (⁶L) Fe^{II}, a Ferrous Heme Bearing Covalently Tethered Axial Pyridine Ligands. *Inorg. Chem.* **2002**, *41*, 2400-2407.